

CONNECTING THE FIRST GALAXIES WITH ULTRA FAINT DWARFS IN THE LOCAL GROUP:
CHEMICAL SIGNATURES OF POPULATION III STARSMYOUNGWON JEON¹, GURTINA BESLA¹ VOLKER BROMM²*Submitted to ApJ*

ABSTRACT

We investigate the star formation history and chemical evolution of isolated analogues of Local Group (LG) ultra faint dwarf galaxies (UFDs; stellar mass range of $10^3 M_\odot < M_* < 10^6 M_\odot$), from the era of the first generation of stars down to $z = 0$, by performing a suite of cosmological hydrodynamic zoom-in simulations. We confirm that reionization, combined with supernova (SN) feedback, is primarily responsible for the truncated star formation in dwarf galaxies. Specifically, haloes with a virial mass of $M_{\text{vir}} \lesssim 2 \times 10^9 M_\odot$ form $\gtrsim 90\%$ of stars prior to reionization. Our work further demonstrates the importance of Population III (Pop III) stars and the associated external metal-enrichment in producing low-metallicity stars ($[\text{Fe}/\text{H}] \lesssim -4$), and for the origin of carbon-enhanced metal-poor (CEMP) stars. We find that dwarf galaxies are composite systems, assembled from multiple progenitor haloes, some of which hosted only Population II (Pop II) stars formed in environments externally enriched by SNe in neighboring haloes. We show that such external enrichment process naturally produces extremely low-metallicity Pop II stars. Our simulations can also reproduce the population of CEMP stars by including Pop III SNe with their intrinsically high $[\text{C}/\text{Fe}]$ yields. We show that α -elements are enhanced at all metallicities, in particular for haloes with $M_{\text{vir}} \lesssim 2 \times 10^9 M_\odot$, implying that the gas in such small dwarfs has preferentially been contaminated by Type II SNe from Pop III and massive Pop II stars. We illustrate how the simulated chemical enrichment can be used to constrain the star formation histories (SFHs) of true observed dwarf galaxies. Our results indicate that observed UFDs lacking stars with $[\text{Fe}/\text{H}] > -1.04$ are likely to have SFHs truncated prior to $z = 3$. Finally, we predict the existence of extremely low-metallicity stars in LG UFD galaxies that preserve the pure chemical signatures of Pop III nucleosynthesis. These predictions can be probed with upcoming deep observations of metal-poor stars in the LG, promising to offer crucial insights into the nature of the first stars and the chemical enrichment history in the early Universe.

Subject headings: cosmology: theory – galaxies: formation – galaxies: high-redshift – dwarf galaxies: Local Group – hydrodynamics – intergalactic medium – stars – abundances

1. INTRODUCTION

One of the biggest challenges in modern cosmology is to understand the first generation of stars and galaxies that formed during the cosmic Dark Ages (see, e.g. Bromm & Yoshida 2011 for a review). They reside in observationally unexplored territory, rendering their detection one of the main goals of the upcoming next-generation facilities, such as the *James Webb Space Telescope (JWST)* (e.g. Gardner 2006) and the 30-40 m giant ground-based telescopes. Recent theoretical studies suggest that the first galaxies were metal-poor and small in size, with a stellar mass of $M_* \lesssim 10^6 M_\odot$. These properties are similar to the faintest dwarf galaxies in the Local Group (LG) (e.g. Greif et al. 2009; Wise et al. 2012; Jeon et al. 2015; Ricotti et al. 2016). In particular, the lowest mass ($M_* \lesssim 10^4 M_\odot$) and most metal-poor ($[\text{Fe}/\text{H}] \lesssim -2$) dwarfs of the LG, known as Ultra Faint Dwarfs (UFDs), have been proposed as possible descendants of the first galaxies and are thus the best place to look for the metal poor stars that hold clues to the nature of the first generation of stars. Studying such systems enables an ap-

proach often termed “galactic archaeology”, wherein local galaxies are used as fossil records of the early assembly history of the Milky Way (MW) (e.g. Salvadori & Ferrara 2009; Frebel et al. 2010; Boylan-Kolchin et al. 2015). Here we illustrate how high resolution cosmological simulations that follow structure formation in the smallest haloes at high redshift can link the first galaxies to their local descendants and identify the chemical signatures of the first generation of stars in the stellar populations of present day UFDs.

The dwarf galaxy satellites of the MW exhibit a great diversity in stellar age, metallicity, and sizes, indicating that they have experienced different star formation histories (SFHs). Specifically, more massive dwarfs ($M_* > 10^6 M_\odot$) are characterized by extended SFHs and show large metallicity spreads, whereas the lower mass UFDs appear to have experienced a truncated SFH, yielding uniformly ancient stellar populations, older than ~ 11 - 12 Gyr (e.g. Bullock et al. 2000; Grebel & Gallagher 2004; Brown et al. 2012; Weisz et al. 2014; Brown et al. 2014).

A plausible mechanism responsible for such early suppression of star formation in UFDs could be reionization, referring to the global phase transition from a neutral Universe to an ionized one at $z = 10 - 6$. During this period of time, the radiation from stars heated the gas in the interstellar medium (ISM) and intergalactic medium

¹ Department of Astronomy, University of Arizona, 933 North Cherry Avenue, Tucson, AZ 85721, USA; my-jeon@email.arizona.edu

² Department of Astronomy, University of Texas, TX 78712, USA

(IGM), thus boosting the Jeans mass, i.e., the minimum mass to trigger gravitational instability, which in turn made it difficult for gas to collapse into haloes (see, e.g. Tolstoy et al. 2009 for a review; and Gnedin & Kravtsov 2006; Bovill & Ricotti 2009; Bovill & Ricotti 2011; Brown et al. 2012).

Significant theoretical progress has been made towards understanding the formation of low mass dwarf galaxies (e.g. Salvadori & Ferrara 2009; Sawala et al. 2010; Munshi et al. 2013; Simpson et al. 2013; Governato et al. 2015; Wheeler et al. 2015; Oñorbe et al. 2015; Fitts et al. 2016). However, the emphasis of these existing studies has been to understand the SFHs of dwarfs and their structural properties at $z = 0$. In particular, work by Wheeler et al. (2015) and Simpson et al. (2013) used cosmological zoom simulations of the formation of low mass galaxies ($M_* \lesssim 10^6 M_\odot$) at high redshift to demonstrate that a combination of stellar feedback and reionization can result in the suppression of star formation in low mass haloes ($M_* \lesssim 10^6 M_\odot$). However, these works did not follow the chemical evolution of individual metal species to low redshift. Existing work concerning the chemical abundances is typically considered in an idealized setting (e.g. Revaz et al. 2009; Corlies et al. 2013; Webster et al. 2014; Webster et al. 2015; Bland-Hawthorn et al. 2015; Revaz et al. 2016). As such, the connection between the stellar populations of LG UFDs and the first generation of stars remains uncertain. We seek to address this major gap in knowledge by self-consistently following the metal enrichment and diffusion from SNe from the first generation of stars in these low mass galaxies, accounting for both reionization and their subsequent hierarchical evolution until the present day.

Ricotti & Gnedin (2005) classify dwarf galaxies based on their SFHs into three categories: galaxies in which the bulk of stars were formed prior to reionization are classified as “true fossils”, whereas “polluted fossils” refer to galaxies that have continuously formed stars beyond reionization, and “survivors” mean galaxies that formed the majority of their stars after reionization. By following the evolution of the first galaxies until the present, we will be able to establish the expected degree of “pollution” in UFDs and furthermore quantify the significance of late time accretion events to their present day chemical properties.

The true fossils in particular, considered as analogues of high- z dwarfs, could offer significant insight on the nature of the first generation of stars, the so-called Population III (Pop III) stars, by preserving their chemical signatures. The first stars are predicted to form out of primordial gas inside minihaloes ($M_{\text{vir}} \sim 10^5 - 10^6 M_\odot$) at $z \gtrsim 15$ (see, e.g. Bromm 2013 for a review; Haiman et al. 1996; Tegmark et al. 1997). The fate of Pop III stars and their chemical signatures depends on their initial mass. Stars in the mass range ($m_{*,\text{Pop III}} = 10 - 40 M_\odot$) ended their lives as core-collapse supernovae (CCSNe) or pair-instability supernovae (PISNe) with a progenitor mass of $m_{*,\text{Pop III}} = 140 - 260 M_\odot$ (e.g. Heger & Woosley 2002). The resulting SN feedback drove the gas out of minihaloes, thus polluting the surrounding IGM with the metals originating in Pop III SNe (e.g. Kitayama & Yoshida 2005; Ritter et al. 2012; Jeon et al. 2014). The second generation, call Population II (Pop II) stars, were born out of the gas thus shaped by Pop III SNe, and, as

a result, they might preserve the chemical signatures of the Pop III stars. Unlike Pop III stars, the lower mass of Pop II stars can allow them to survive until today.

Therefore, investigating the chemical abundance patterns of Pop II stars can inform us of the typical SFHs experienced by UFDs. In particular, the abundances of alpha elements compared to iron can tell us about the timescale over which stars have formed and about the corresponding star formation efficiency. For example, alpha-elements such as Si, Mg, Ca, and Ti are more abundant relative to iron in Type II SNe from massive stars, whereas iron dominates over alpha elements when Type Ia SNe are triggered (Tinsley 1979). Owing to the long lifetime of low-mass stars, the onset of Type Ia SNe is delayed, on the order of ~ 100 Myr or longer after star formation begins. Consequently, the enhanced $[\alpha/\text{Fe}]$ ratios from Type II SNe decline with increasing $[\text{Fe}/\text{H}]$, as stars begin to form in gas clouds that are metal-enriched by Type Ia SNe after $\gtrsim 100$ Myr.

This trend is also applicable to star formation in the early Universe. The mass range of Pop III stars is still uncertain, but recent statistical studies of first star formation have predicted massive stars with a broad range from a few tens to a few $1000 M_\odot$ (e.g. Hirano et al. 2014; Hirano et al. 2015). As a consequence, Pop III stars were likely to die as Type II SNe rather than Type Ia, leading to an enhancement in $[\alpha/\text{Fe}]$ ratios. These chemical peculiarities are expected to be preserved in the subsequent generation of stars. Reionization additionally “froze in” any such signatures: if further star formation was terminated by reionization in high- z dwarfs, their SFHs would extend over ~ 500 - 600 Myr, which is too short for Type Ia SNe to become the dominant source of metals.

To date, a complete theoretical understanding of chemical abundances in UFD stellar populations, in the full cosmological context, and considering the detailed enrichment from early Pop III and Pop II stars, is still lacking. This study is the first to self-consistently follow these processes from high redshift to the present day, allowing us to constrain the expected signatures of Pop III stars in the stellar populations of current UFDs.

Here, we present the results of a suite of cosmological, high-resolution zoom-in simulations that trace the chemical and mass evolution of low mass dwarf galaxies (UFD mass analogs) from high redshifts down to $z = 0$. In this work, we have two main goals: (1) to investigate the role of reionization and SNe feedback in the SFHs of UFD analogs; and (2) to compare the resulting stellar abundance patterns with observational data from present day UFDs, highlighting signatures of chemical enrichment from Pop III stars. We will discuss the structural properties of the simulated dwarfs (e.g. velocity dispersions and sizes) in an upcoming paper. The most important difference of this work from previous studies is the ab-initio inclusion of early star formation and enrichment. In addition, for the first time, we derive detailed chemical abundance patterns for individual stars from realistic cosmological simulations, to be compared with stellar archaeological data. Our hydrodynamical simulations are nicely complemented by the recent dark matter-only investigation of Griffen et al. (2016). Both treatments employ cosmological initial conditions, with the latter focusing on representing the realistic large-scale density field of the LG environment, while our work includes the de-

tailed physics of the baryonic component. Corlies et al. 2017 (priv. comm.) consider the SFHs and metallicity distribution functions of a range of halos within a fully simulated cosmological box as opposed to zooming in on specific halos. However, the computationally intensive feedback methods implemented restrict the simulation to a small volume and can only be run to $z=7$.

The outline of the paper is as follows. Our numerical methodology is described in Section 2, and the simulation results are presented in Section 3. We discuss the limitations of this work in Section 4. Finally, our main findings are summarized in Section 5. For consistency, all distances are expressed in physical (proper) units unless noted otherwise.

2. NUMERICAL METHODOLOGY

2.1. Simulation Set Up

We have performed a suite of hydrodynamic zoom-in simulations using a modified version of the *N*-body/TreePM Smoothed Particle Hydrodynamics (SPH) code GADGET (Springel et al. 2001; Springel 2005). As cosmological parameters, we adopt a matter density of $\Omega_m = 1 - \Omega_\Lambda = 0.265$, baryon density of $\Omega_b = 0.0448$, present-day Hubble expansion rate of $H_0 = 71 \text{ km s}^{-1} \text{ Mpc}^{-1}$, a spectral index $n_s = 0.963$, and a normalization $\sigma_8 = 0.801$. The initial conditions are generated using the cosmological initial conditions code MUSIC (Hahn & Abel 2011). As a preliminary run, we perform a dark matter only using 128^3 particles in a $L = 6.25h^{-1}$ comoving Mpc box. Then, we identify six galaxies with a mass of $M_{\text{vir}} \sim 10^9 M_\odot$ at $z = 0$ around a MW-size halo ($M_{\text{vir}} \sim 2 \times 10^{12} M_\odot$) (see, Figure 1). We conduct four consecutive refinements for all particles within $\sim 2R_{\text{vir}}$ of the selected low mass haloes at $z = 0$, where R_{vir} is a virial radius, as marked in Figure 1, defined as the radius at which the mass density is 200 times higher than the average density of the Universe. The resultant effective resolution is 2048^3 , giving rise to dark matter (DM) and gas masses in the most refined region of $m_{\text{DM}} \approx 2000 M_\odot$ and $m_{\text{SPH}} \approx 495 M_\odot$, respectively. The properties of the selected haloes in the different zoom-in regions are listed in Table 1.

We find that in order to minimize computational cost, we preferentially choose haloes in relatively isolated regions, distributed from 0.6 Mpc to 2.1 Mpc from the center of the MW-size halo, which is illustrated as the largest white circle in the left panel of Figure 1. This choice naturally allows us to exclude other possible processes that might affect the SFHs and chemical properties of the dwarfs, such as tidal interactions and ram-pressure stripping. We fix the softening lengths for DM and star particles as $\epsilon_{\text{DM}} = 40 \text{ pc}$ at all redshifts. We use adaptive softening length for the gas particles, where the softening length is proportional to the SPH kernel length with a minimum value of $\epsilon_{\text{gas,min}} = 2.8 \text{ pc}$.

2.2. Chemistry, Cooling, and UV Background

We solve the coupled, non-equilibrium rate equations every time-step for the primordial chemistry from nine atomic and molecular species ($\text{H}, \text{H}^+, \text{H}^-, \text{H}_2, \text{H}_2^+, \text{He}, \text{He}^+, \text{He}^{++}$, and e^-), as well as from the three deuterium species D, D^+ , and HD (Glover & Jappsen 2007) in the presence of the cosmic

UV/X-ray background provided by Haardt & Madau (2012). The UV background is implemented in terms of ionization and heating rates of H I , He I and He II as a function of redshift. Such background is an important factor in influencing the SFHs, in that the early presence of UV radiation is likely to suppress star formation early on. Here, we begin to include a UV background at $z = 7$, and linearly increase its strength until $z = 6$. At lower redshifts, we incorporate the background at full amplitude, assuming that reionization is complete at $z = 6$ (e.g. Gunn & Peterson 1965; Fan et al. 2006).

Self-shielding of the dense gas is included such that the UV background is attenuated as a function of $\exp(-N_{\text{H I}} \bar{\sigma}_{\text{ion}})$, where $N_{\text{H I}} = x n_{\text{H I}}$. Here, $x = h$ is the SPH kernel size, $n_{\text{H I}}$ the neutral hydrogen number density, and $\bar{\sigma}_{\text{ion}}$ the frequency-averaged photoionization cross-section for H I . In addition, the photodissociation of molecular hydrogen, H_2 , by the UV radiation in the Lyman-Werner (LW) band (11.2 eV–13.6 eV) is considered (e.g. Abel et al. 1997), with a rate $k_{\text{LW}} = 1.38 \times 10^{-12} \text{ s}^{-1} J_{21}$. Here, the normalized LW mean intensity is $J_{21} = \bar{J}_\nu / (10^{-21} \text{ erg Hz}^{-1} \text{ s}^{-1} \text{ cm}^{-2} \text{ sr}^{-1})$, with $\bar{J}_\nu(z)$ being the average mean intensity in the LW band, calculated from the spectra in Haardt & Madau (2011). The treatment for photodissociation of deuterated hydrogen HD is identical to that of H_2 .

We consider all relevant primordial cooling processes such as H and He collisional ionization, excitation and recombination cooling, bremsstrahlung, inverse Compton cooling, and collisional excitation cooling of H_2 and HD . Additionally, gas cooling by metal species such as carbon, oxygen, silicon, magnesium, neon, nitrogen, and iron is taken into account under equilibrium conditions. Specifically, we employ the method implemented by Wiersma et al. (2009), where the cooling rates are computed element-by-element from pre-computed tables based on the photo-ionization code CLOUDY (Ferland et al. 1998), by interpolating the value as a function of density, temperature, and metallicity. Note that we ignore H_2 formation via dust and also dust cooling for the following reasons: (1) at high redshifts, $z > 7$, the amount of dust is not sufficient to be a dominant source of H_2 formation, particularly in small systems ($M_* \lesssim 10^6 M_\odot$); and (2) at low redshifts, metal cooling dominates over H_2 cooling.

2.3. Star Formation Physics

The Pop III initial mass function (IMF) is still a subject of debate (e.g. Bromm 2013). The final mass of Pop III stars is determined by the complex interplay between protostellar UV feedback, gas accretion through a self-gravitating circumstellar disk, and its fragmentation via gravitational instability (e.g. McKee & Tan 2008; Hosokawa et al. 2011; Stacy et al. 2012). Recent 2-D and 3-D radiation hydrodynamic simulations, including stellar feedback from a protostar, predict that the mass of Pop III stars is broadly distributed from $m_* \lesssim 1 M_\odot$ to $m_* \sim 1000 M_\odot$ (e.g. Hirano et al. 2014; Susa et al. 2014; Hosokawa et al. 2016; Stacy et al. 2016). The statistical study by Hirano et al. (2015) suggests that the characteristic mass of Pop III stars also sensitively depends on the photo-dissociation from external far-UV (FUV) radiation, emitted by neighboring Pop III stars.

TABLE 1
CHARACTERISTICS OF THE SIMULATED UFD ANALOGS AT $z = 0$.

Halo	M_{vir}	r_v	M_*	D_h	f_b	$r_{1/2}^*$	[Fe/H]	$[\alpha/\text{Fe}]$	σ_*	SF _{trun}
Unit	[$10^9 M_\odot$]	[kpc]	[$10^4 M_\odot$]	[Mpc]	[%]	[pc]	-	-	[km s^{-1}]	-
halo1	1.53	23.7	4.3	0.6	0.08	345	-2.63	0.52	6.4	Yes
halo2	1.53	23.5	3.8	2.0	0.07	320	-2.25	0.44	6.0	Yes
halo3	1.60	23.9	8.2	2.1	0.1	296	-2.28	0.52	6.7	Yes
halo4	2.21	26.6	13.0	1.9	0.96	513	-2.45	0.54	11.2	No
halo5	3.15	29.9	20.0	0.9	0.05	479	-2.27	0.53	9.9	No
halo6	3.95	32.1	88.6	3.7	0.1	438	-1.23	0.47	11.6	No

NOTE. — First row denotes the derived physical quantities of the galaxies. First column indicates the name of haloes at each zoom-in region. Column (2): viral mass in $10^9 M_\odot$. Column (3): virial radius in kpc. Column (4): stellar mass in $10^4 M_\odot$. Column (5): distance from a MW like host halo in Mpc. Column (6): baryon fraction in %. Column (7): half stellar mass radius in pc. Column (8): average iron-to-hydrogen ratios of stars. Column (9): average alpha-to-iron ratios of stars. Column (10): stellar velocity dispersion in km s^{-1} . Column (11): truncated star formation after reionization.

Due to the limited numerical resolution, individual stars cannot be resolved, and we instead allow Pop III stars to form as a single star cluster. We assume a top-heavy IMF with a functional form of $\phi_{\text{Pop III}}(m) = dN/d\log m \approx m^{-\alpha}$, a slope of $\alpha = 1$, and a mass range of $[m_0, m_1] = [10, 150] M_\odot$. Once a gas particle exceeds a threshold density of $n_{\text{H,th}} = 100 \text{ cm}^{-3}$, the highest-density SPH particle is converted into a collisionless star particle with a 100% conversion efficiency, forming $M_* \approx 500 M_\odot$ in Pop III stars at once. We note that the adapted threshold density is somewhat lower than the characteristic value, $n_{\text{H,th}} = 10^4 \text{ cm}^{-3}$, where gravitational instability is triggered in primordial star formation (e.g. Bromm et al. 2002; Abel et al. 2002). In an effort to reduce computational cost, we avoid implementing such a higher threshold density. However, our choice of $n_{\text{H,th}} = 100 \text{ cm}^{-3}$ is reasonable given that, above $n_{\text{H}} = 10^3 \text{ cm}^{-3}$, the Pop III star formation time is insensitive to any further increase in threshold density (Muratov et al. 2013).

Stars are formed from gas clouds at a rate $\dot{\rho}_* = \rho_{\text{th}}/\tau_*$, where $\tau_* = \tau_{\text{ff}}/\epsilon_{\text{ff}}$ is the star formation time scale, $\tau_{\text{ff}} = [3\pi/(32G\rho_{\text{th}})]^{1/2}$ the free fall time at the threshold density ρ_{th} , and ϵ_{ff} the star formation efficiency per free fall time (Schmidt 1959). The star formation efficiency for Pop III stars has yet to be pinned down precisely (e.g. Hirano et al. 2015; Stacy et al. 2016). Using a global baryon fraction of $f_b = 0.168$, we set $\epsilon_{\text{ff,Pop III}} = M_{\text{char,Pop III}}/(M_{\text{vir}} \times f_b)$, where $M_{\text{char,Pop III}}$ is the characteristic mass of Pop III stars, leading to $\epsilon_{\text{ff,Pop III}} \sim 0.01$. We note that this value is similar to a typical efficiency in local star formation. Then, an SPH particle is stochastically converted into a collisionless star particle in a time interval Δt , if a random number is smaller than $\min(\Delta t/\tau_*, 1)$, to follow a given distribution $\dot{\rho}_* = \rho_{\text{th}}/\tau_*$. The star formation timescale is then given by

$$\tau_* = \frac{\tau_{\text{ff}}(n_{\text{H,th}})}{\epsilon_{\text{ff}}} \sim 400 \text{ Myr} \left(\frac{n_{\text{H,th}}}{100 \text{ cm}^{-3}} \right)^{-1/2}. \quad (1)$$

Once pristine gas is enriched with metals dispersed by SN explosions of the first generation of stars, low-mass, long-lived second generation Pop II stars are formed out of the metal-polluted gas clouds. For Pop II star

formation, we employ the same star formation recipe as for Pop III, with an identical star formation efficiency, $\epsilon_{\text{ff,Pop II}} = 0.01$, but adding an additional metallicity criterion. If the metallicity of a gas particle, eligible for star formation, exceeds the critical metallicity, $Z_{\text{crit}} = 10^{-5.5} Z_\odot$, for the transition from Pop III to Pop II, we form a Pop II star cluster. The choice of $Z_{\text{crit}} = 10^{-5.5} Z_\odot$ is motivated by dust-continuum cooling (e.g. Omukai 2000; Schneider & Omukai 2010; Bromm et al. 2001; Safranek-Shrader et al. 2016), where dust cooling is responsible for further gas fragmentation at high densities, $n_{\text{H}} \gtrsim 10^{16} \text{ cm}^{-3}$, enabling the formation of low-mass stars. For the Pop II IMF, we use a Chabrier IMF over the mass range of $[0.1 - 100] M_\odot$.

2.4. Chemical Feedback

In this section, we describe how we implement stellar yields from SN explosions and metal diffusion into the ISM and IGM. We use an implementation of chemodynamics where enrichment by winds from asymptotic giant branch (AGB) stars, and by Type II and Type Ia SNe are incorporated (Wiersma et al. 2009). At every time step, the mass of 11 individual elements from dying stars is computed and released into the neighboring medium, followed by subsequent diffusive mixing in the ISM and IGM. We have, for the first time, applied the metal diffusion scheme to understand the evolution of chemical abundances of dwarf galaxies in the full cosmological context. We briefly outline the procedure here.

2.4.1. Stellar Yields: Population III Stars

The low atmospheric opacities due to the absence of metals renders mass loss by stellar winds from primordial stars almost negligible (e.g. Kudritzki & Puls 2000). Therefore, the final fate of Pop III stars is determined by their initial mass. For example, massive stars in the mass range between $10 M_\odot$ and $40 M_\odot$ end their lives as conventional CCSNe, some of which are hypernovae in the range of $25 M_\odot \lesssim m_* \lesssim 40 M_\odot$. Very massive stars within the particular mass range of $140 M_\odot \lesssim m_* \lesssim 260 M_\odot$ are expected to experience PISNe, powered by electron-positron pair creation. In the latter case, after central helium burning, the core temperature becomes sufficiently high to abundantly produce electron-positron pairs, such that the star begins to collapse due to the

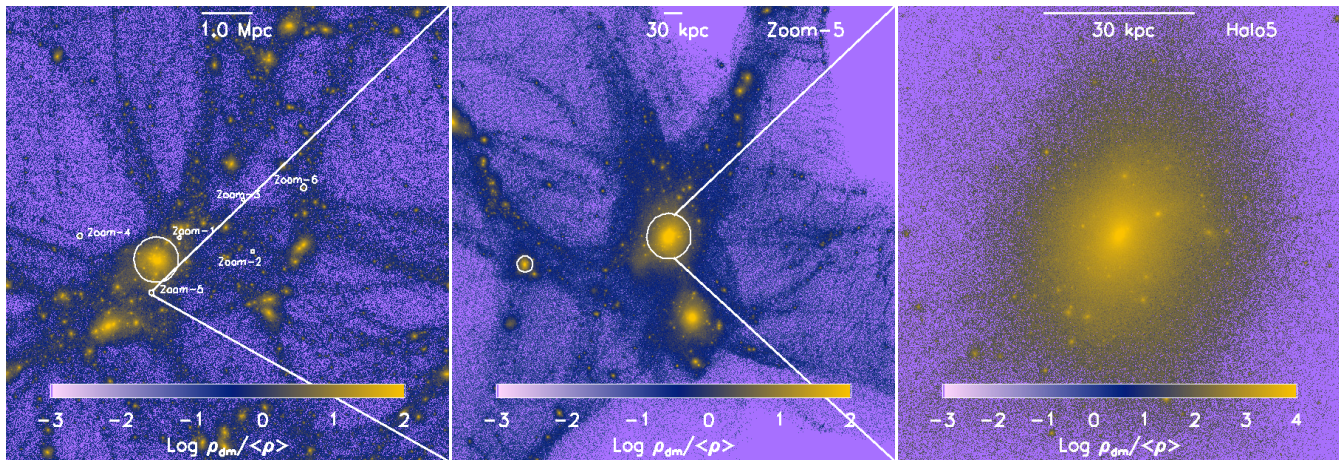


FIG. 1.— Dark matter distribution on progressively smaller scales at $z = 0$, as labeled on each panel. White lines denote the region to be depicted in the next-smallest scale. *Left*: Final simulation output from the dark-matter only preliminary run that includes a MW like halo with a mass of $M_{\text{vir}} \sim 2 \times 10^{12} M_{\odot}$, shown as the halo surrounded by the largest white circle. Six different zoomed-in regions around the central host halo are also presented as small white circles. *Middle*: DM distribution of the selected zoom-in region. There are two haloes in the refined region including the most massive halo, HALO5, which is zoomed in the right panel. *Right*: Detailed look of HALO5. The virial radius of the halo is ~ 30 kpc at $z = 0$.

sudden drop in radiation pressure support. The rapid contraction in turn triggers implosive oxygen and silicon burning which produces enough energy to completely disrupt the star, leaving no remnant behind. If Pop III stars are more massive than $m_* > 260 M_{\odot}$, they are expected to undergo direct collapse into a black hole without any explosion since the thermonuclear energy release is not sufficient to reverse the implosion.

Nucleosynthetic yields of CCSNe from Pop III progenitor stars and their remnant masses are provided by Heger & Woosley (2010), comprising progenitor masses of $10 - 100 M_{\odot}$, and exploring a range of explosion energies between 0.3×10^{51} erg and 10^{52} erg. Specifically, we use yields for SN explosion energy of 1.2×10^{51} erg, in the absence of rotation. For PISNe, we adapt the yields given in Heger & Woosley (2002). It should be noted that the effects of stellar rotation and magnetic fields are not considered. E.g., some recent studies suggest that under the influence of stellar rotation the lowest mass resulting in a PISN can be shifted down to $75 M_{\odot}$ (e.g. Chatzopoulos & Wheeler 2012).

2.4.2. Stellar Yields: Population II Stars

Stars experience strong mass loss at the end of their lives, corresponding to the AGB or SN phase. The lifetime of a star is defined as the time when a star leaves the main-sequence and enters its red giant phase. Here, we employ metallicity-dependent tables of stellar lifetimes, covering values from $Z = 0.0004$ to $Z = 1.0$ (Portinari et al. 1998). Intermediate-mass stars ($0.8 M_{\odot} \lesssim m_* < 8 M_{\odot}$) lose up to 60% of their mass during the terminal AGB stage. The corresponding yields are taken from Marigo (2001), where stars as massive as $5 M_{\odot}$ are covered. Due to the low wind velocity compared to the velocity dispersion in the ISM, the kinetic energy input from AGB winds is neglected.

Substantial amounts of metals are ejected by Type II SNe when massive stars ($m_* \gtrsim 8 M_{\odot}$) explode at the end of their life. The yields from Type II SNe are from Portinari et al. (1998), in which mass loss on the main sequence is considered. They provide a yield set that

is derived in a self-consistent manner with the AGB yields, in terms of stellar lifetimes and mass range considered. Due to our short hydrodynamic timesteps, $\Delta t = 0.01 - 0.1$ Myr, compared to the timescale over which Type II SNe occur, metals are released through multiple timesteps after the most massive star in a stellar cluster undergoes a SN explosion, followed by subsequent explosions of less massive stars. The energy associated with Type II SNe is distributed onto neighboring particles as thermal energy, comprising a total of $E_{\text{SN,Pop II}} = 8.6 \times 10^{51}$ erg. This value is obtained by integrating over a Chabrier IMF in the mass range of $[6, 100] M_{\odot}$ for a Pop II cluster. The SN energy is deposited at once in a single time step at the end of the most massive star’s life in a Pop II cluster. A detailed description is to follow in Section 2.5.

The progenitor mass of a Type Ia SN is thought to be between $3 M_{\odot}$ and $8 M_{\odot}$. Once the mass of a white dwarf remnant exceeds the Chandrasekhar mass, either by mass transfer from a companion star or the merger of two white dwarfs, a Type Ia SN is triggered. Due to the large uncertainty attributed to the details of binary evolution, determining the Type Ia SN rate is highly complex, compared to the mass release by Type II SNe and AGB stars, where mass loss simply occurs at the end of the progenitor’s life. We employ empirical delay time functions (e.g. Barris & Tonry 2006; Förster et al. 2006), expressed as e-folding times, $\eta(t) = e^{-t/\tau_{\text{Ia}}}/\tau_{\text{Ia}}$ where $\tau_{\text{Ia}} = 2$ Gyr is the characteristic delay time. The SN Ia rate at a given timestep Δt is then $N_{\text{SN Ia}}(t; t + \Delta t) = a \int_t^{t+\Delta t} f_{\text{wd}}(t') \eta(t') dt'$, where $a = 0.01$ is a normalization parameter and f_{wd} is the number of stars that have evolved into white dwarfs per unit stellar mass (Mannucci et al. 2006). The Type Ia SN yields, based on the explosion of a Chandrasekhar-mass carbon-oxygen white dwarf, are taken from the spherically symmetric “W7” model (Thielemann et al. 2003). The corresponding SN energy is again distributed onto neighboring particles as thermal energy, but this feedback is likely to be less effective in disturbing the surrounding gas because the energy injection is distributed over billions of years.

2.4.3. Metal Diffusion

After metals from AGB stellar winds, from Type II and Type Ia SNe, and from PISNe are released, they should be transported into the ISM and IGM. However, owing to the lack of intrinsic mass flux between SPH particles, the implementation of metal transfer in SPH simulations is nontrivial. Commonly, a “particle metallicity” has been widely used, where metals are locked up into the initial neighboring gas particles, resulting in a very compact metal distribution around a SN explosion site. A new improved implementation has been suggested by Wiersma et al. (2009), where gas metallicity is computed in terms of density $Z_{\text{sm}} = \rho z / \rho$. This smoothed metallicity is suitable in simulating galaxy formation because gas cooling, one of the key factors in star formation, depends on gas density. Thus using the smoothed metallicity, derived with the SPH kernel formalism, allows one to compute metallicity-dependent gas cooling in a more consistent way. Also, the smoothed metallicity partially accounts for the spreading of metals. The method we adopt here, on the other hand, is a diffusion-based metallicity implemented by Greif et al. (2009), where the mixing efficiency on unresolved scales is determined by the physical properties on the scale of the SPH smoothing kernel (Klessen & Lin 2003).

Initially, the ejected metals are distributed among the neighboring gas particles, $N_{\text{ngb}} = 48$, giving rise to initial particle metallicities,

$$Z_i = \frac{m_{\text{metal},i}}{m_{\text{SPH}} + m_{\text{metal},i}}. \quad (2)$$

Then, the metals are transported by solving the diffusion equation, written in the form,

$$\frac{dc}{dt} = \frac{1}{\rho} \nabla \cdot (D \nabla c), \quad (3)$$

where c is the concentration of a fluid per unit mass, corresponding to the total gas metallicity in this work. We also track individual metal species element-by-element such as C, O, Si, Mg, Ne, Ni, and Fe. D is the diffusion coefficient defined as $D = 2 \rho \tilde{v} \tilde{l}$, where the length scale, \tilde{l} , is comparable to the smoothing length of the SPH kernel, $\tilde{l} = h$, and ρ is the gas density. The velocity dispersion within the kernel, \tilde{v} , is given by

$$\tilde{v}_i^2 = \frac{1}{N_{\text{ngb}}} \sum_j |v_i - v_j|^2. \quad (4)$$

Here, v_i and v_j are the velocities of particles i and j within the kernel. Efficient metal mixing is achieved owing to the increased velocity dispersion of the gas as the forward shock from a SN explosion passes by. It should be mentioned that this method assumes that motions in the resolved scales cascade down to unresolved scales within which the gas is homogeneously mixed. The resulting velocity field is driven by a homogeneously and isotropically turbulent medium, meaning that three-dimensional structures within the medium are not considered.

2.5. Thermal Feedback

During the main-sequence stage, Pop III and Pop II stars emit photons that ionize and heat the surrounding medium, but in this work, we do not include photoheating and radiation pressure from stars for the sake of feasibility. It would be computationally prohibitive to follow galaxy evolution over time down to $z = 0$, while self-consistently solving the radiative transfer equation for our highly-resolved star forming regions. Once a massive Pop III or Pop II star dies, exploding as a Type II SN, the explosion energy is injected into the surrounding medium, destroying dense gas, and thus suppressing subsequent star formation. Here, we insert SN energy as thermal energy, distributed onto neighboring gas particles. The common problem regarding the thermal energy method is that gas particles heated by a SN explosion radiate their energy away too quickly, before making SN feedback effective. This is in part due to the unphysical absence of photoheating in our current simulations, which would otherwise act to photoevacuate gas prior to the SN explosion, rendering the surrounding medium too dense.

Another problem is that SN energy is deposited onto too much gas mass, owing to the limited resolution. In reality, one CCSN is triggered out of every $\sim 100 M_{\odot}$ in stars, and the SN energy is carried by $\ll 100 M_{\odot}$ of ejecta, while in cosmological simulations the mass of neighboring gas particles that receive the SN energy is much larger than the physical ejecta mass. Consequently, temperatures in the heated gas remain below $T \sim 10^6$ K, where the cooling time is too short. Therefore, one widely used way to circumvent the over-cooling problem is disabling gas cooling for a few tens of Myr. In our simulations, on the other hand, we follow the strategy proposed by Dalla Vecchia & Schaye (2012), which assigns temperatures above $10^{7.5}$ K to the heated particles, thus preventing the gas from radiatively losing its energy too quickly. We briefly summarize this approach here.

The temperature jump of gas particles that receive SN energy is given by

$$\begin{aligned} \Delta T &= (\gamma - 1) \frac{\mu m_{\text{H}}}{k_{\text{B}}} \epsilon_{\text{SN}} \frac{M_{*}}{m_{\text{g,heat}}} \\ &= 4.34 \times 10^7 \text{ K} \left(\frac{n_{\text{SN}}}{1.736 \times 10^{-2} M_{\odot}^{-1}} \right) \left(\frac{\mu}{0.6} \right) \\ &\quad \times E_{51} \frac{M_{*}}{m_{\text{g,heat}}}, \end{aligned} \quad (5)$$

where $\epsilon_{\text{SN}} = n_{\text{SN}} E_{51} \times 10^{51} \text{ erg}$ is the total available SN energy per unit stellar mass and $E_{51} \times 10^{51} \text{ erg}$ ($E_{51} = 1$) is the available energy from a single CCSN event. The number of stars per unit stellar mass ending their lives as Type II SNe is defined as $n_{\text{SN}} = \int_{m_0}^{m_1} \phi(m) dm$ where m_0 and m_1 are the minimum and maximum initial mass of stars eligible for SN explosion, and $\phi(m)$ is a given IMF. For Pop III clusters, the number densities of CCSNe and PISNe per stellar mass are $n_{\text{CCSN,Pop III}} = 1.2 \times 10^{-2} M_{\odot}^{-1}$ ($[m_0, m_1] = [11, 40] M_{\odot}$) and $n_{\text{PISN,Pop III}} = 4.3 \times 10^{-3}$ ($[m_0, m_1] = [140, 260] M_{\odot}$), respectively. The latter means that typically two PISN events happen in the $500 M_{\odot}$ Pop III cluster, $N_{\text{PISN}} = n_{\text{PISN,Pop III}} M_{*,\text{Pop III}} \sim 2$. For

Pop II clusters with the assumed Chabrier IMF, the number density of CCSNe is $n_{\text{CCSN,Pop II}} = 1.73 \times 10^{-2} M_{\odot}^{-1}$ ($[m_0, m_1] = [8, 100] M_{\odot}$). The total available SN energy from a single Pop III and Pop II cluster is $E_{\text{SN}} = (\epsilon_{\text{CCSN,Pop III}} + \epsilon_{\text{PISN,Pop III}}) \times M_{*,\text{Pop III}} = 2.75 \times 10^{52}$ erg, where $\epsilon_{\text{PISN,Pop III}} = n_{\text{PISN,Pop III}} \times 10^{52}$ ergs, and $\epsilon_{\text{CCSN,Pop II}} \times M_{*,\text{Pop II}} = 8.5 \times 10^{51}$ erg, respectively. In order to assure that the heated gas reaches above 10^7 K, making the thermal SN feedback effective in the surrounding medium, we release the SN energy at once when the most massive star in a cluster undergoes a SN explosion.

In the standard SPH thermal feedback implementation, SN energy is normally distributed onto neighboring SPH particles, where $N_{\text{neigh}} = 48$. If we heat all the neighboring particles, then the total heated gas mass is $m_{\text{g,heat}} = m_{\text{SPH}} N_{\text{neigh}} = 2.3 \times 10^4 M_{\odot}$ and it renders the ratio $M_*/m_{\text{g,heat}} = 0.02$ for the Pop III and Pop II clusters. Consequently, the neighboring gas particles would achieve a temperature jump lower than $\Delta T \sim 10^{7.5}$ K by an order of magnitude, making SN feedback incapable of impacting the gas. In order to increase the temperature jump, we decrease the ratio $M_*/m_{\text{g,heat}}$ by reducing the number of neighboring heated particles to a single particle, the closest one around a stellar cluster. Heating a single gas particle ensures the ratio $M_*/m_{\text{g,heat}}$ to be of order unity.

Additionally, we use a timestep-limiter such that the ratio of timesteps of neighboring SPH particles cannot be larger than a given factor, here adopting a value of 4 (Saitoh & Makino 2009; Durier & Dalla Vecchia 2012). The implementation is essential for the correct treatment of SN explosions, especially for high resolution multiphase simulations with individual time-steps, where the hot gas ($T > 10^{7.5}$ K) is located near cold, dense gas ($T < 10^4$ K), resulting in a large difference in their timesteps that eventually could lead to a large integration error. Also, we consider a timestep-update where all neighboring particles around a SN explosion site become active particles at the time of energy injection (Dalla Vecchia & Schaye 2012), allowing them to immediately react to a sudden SN event.

3. SIMULATION RESULTS

In the following, we present our simulation results concerning the chemical properties of low mass reionization relics, in comparison to the observed properties of UFD galaxies about the MW. In Section 3.1, we consider the star formation history of the simulated galaxies over cosmic time down to $z = 0$, followed by a discussion of the residual gas in the isolated UFD analogs at $z = 0$ in Section 3.2. Then, we explain the general trend of metal yields from Pop III and Pop II stars in Section 3.3, and the resulting chemical abundances of the UFDs in Section 3.4. We further discuss how to provide insight into the SFHs and accretion timescales of the observed LG UFDs by comparing with our simulated UFD analogs. Finally, in Section 3.6, we present the global galaxy properties at $z = 0$ and compare our results with other theoretical studies and observations. All the simulated dwarfs reside at distances from 0.6–3.7 Mpc from the central galaxy at $z = 0$ (see, Figure 1). As such, environmental factors (tides, ram pressure stripping, UV from central

galaxy), therefore, are not relevant to the evolution of these galaxies.

3.1. Star Formation History

Figure 2 shows the time evolution of the zoomed-in low mass haloes (UFD mass analogs) in each refined region (*clockwise from upper left-hand*): the total and gas mass, the maximum hydrogen number density, cumulative fractional SFH, and star formation rate (SFR). These quantities are computed based on the properties of particles within the virial volume of the haloes. Most of the haloes begin to grow from minihaloes with a mass of $M_{\text{vir}} = 10^5 - 10^6 M_{\odot}$ at $z \gtrsim 15$, inside of which early Pop III stars form. The emergence of first star formation differs from halo to halo: the lower the halo mass, the later Pop III stars begin to form. This is because a halo must reach a minimum mass required to host gas with a molecular hydrogen fraction of $f_{\text{H}_2} \gtrsim 10^{-4}$, above which H_2 cooling is efficient (e.g. Tegmark et al. 1997; Bromm et al. 2002). We see that Pop III stars emerge at $z \lesssim 11$ in the less massive haloes (HALO1, HALO2), while the more massive haloes (HALO4, HALO5, HALO6) commence Pop III star formation before $z = 15$. The final virial masses at $z = 0$ are less than $M_{\text{vir}} \sim 1.6 \times 10^9 M_{\odot}$ for three haloes HALO1, HALO2, HALO3, while the others are slightly more massive with $M_{\text{vir}} \sim 2.1 \times 10^9$ (HALO4), $M_{\text{vir}} \sim 3.1 \times 10^9 M_{\odot}$ (HALO5), and $M_{\text{vir}} \sim 4 \times 10^9 M_{\odot}$ (HALO6), respectively.

We point out that early on, prior to reionization, star formation proceeds in an episodic fashion. This is a consequence of regulated star formation: the gas within the shallow potential well of a dwarf can easily be disrupted and evacuated by SN feedback, and it takes time for the halo gas to be replenished. This time delay gives rise to the episodic, bursty star formation with timescale of the order of a few ~ 10 Myr. As explained in Section 2, we gradually increase the external UV background, starting from $z = 7$ to its full strength by $z = 6$, indicated by the grey shaded vertical region in Figure 2; afterwards, the background is present at full amplitude down to $z = 0$.

The star formation history of the simulated galaxies strongly depends on their halo mass. Quenching of star formation by reionization is clearly reflected in the noticeable drops in SFR during $z \sim 7 - 6$ in the less massive haloes, HALO1, HALO2, and HALO3. Among them, HALO1 continues to form stars for about ~ 30 Myr beyond $z = 7$, while HALO2 and HALO3 exhibit sharply truncated star formation as soon as the UV background is introduced. This residual star formation in HALO1 is due to the existence of dense gas, self-shielded from the UV background. Although two other haloes, HALO4 and HALO5, also experience SFR quenching by the UV background, we see a rebirth of star formation at late epochs, below $z = 4$. It turns out that gas inflow in HALO5 is driven by mergers with other haloes at $z \sim 1.8$, such that the primary progenitor of HALO5 grows in mass by a factor of 5, leading to the ignition of star formation at $z \lesssim 0.5$. HALO4 shows late starbursts at $z \sim 3.9$ and $z \sim 0$, as well.

Interestingly, the most massive halo (HALO6) overcomes the effect of negative feedback from UV photoheating, since the halo already reaches a mass of $M_{\text{vir}} = 2.5 \times 10^8 M_{\odot}$ at $z = 7$, which is massive enough to not be significantly affected by external radiation. Therefore,

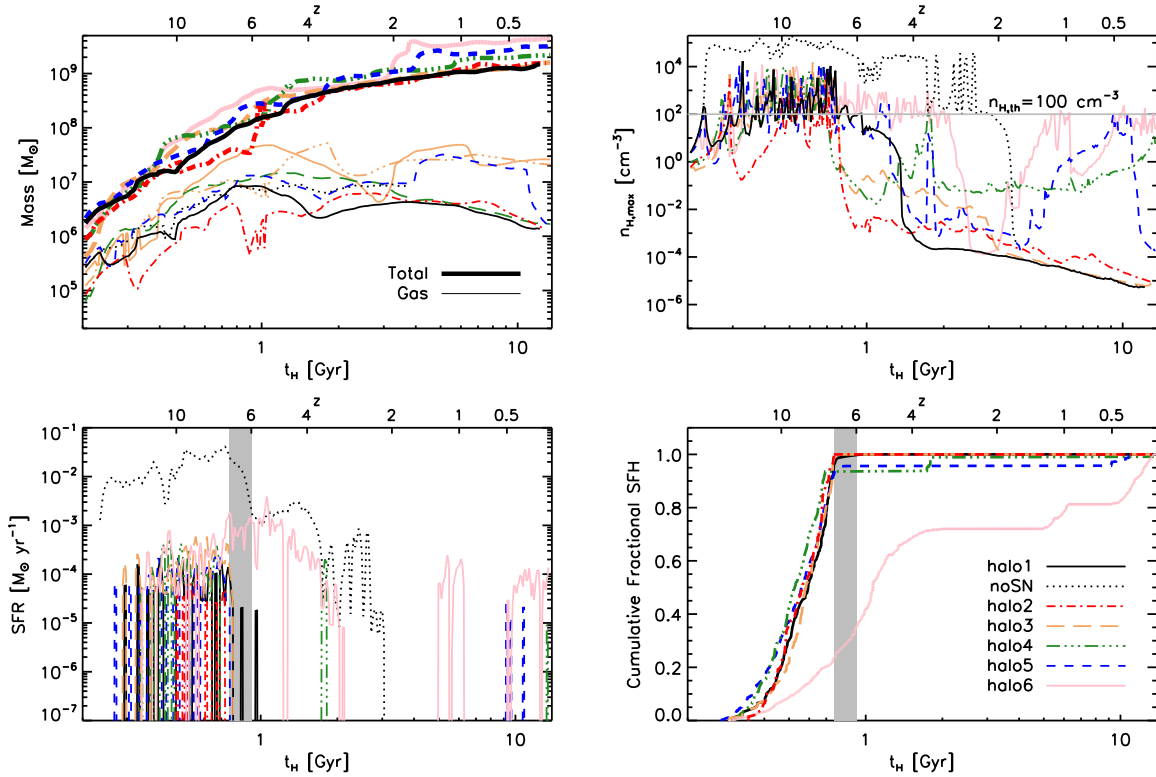


FIG. 2.— Time evolution of the UFD analogs, i.e. the most massive haloes, from the zoomed-in regions. *Clockwise from upper left:* total and gas mass, the maximum hydrogen density, cumulative fractional star formation history, and star formation rates within the virial radius of the haloes. The UV background is introduced at $z = 7$ starting from zero strength and gradually increasing to the full amplitude at $z = 6$, depicted as the grey shaded region in the bottom plots. Different colors and line types indicate the evolution of each UFD analog. The dotted line indicates results when no SN feedback is included in the case of HALO1. Relatively less massive haloes (HALO1, HALO2, and HALO3), whose halo mass is less than $2 \times 10^9 M_\odot$ ($z = 0$), form *all* stars prior to reionization. On the other hand, in HALO4 and HALO5, late starbursts are triggered mainly driven by mergers with other haloes. The most massive halo, HALO6, forms only about 30% of stars before reionization and star formation is continuously triggered under the influence of the UV background. Star formation continues well past $z = 6$, illustrating that reionization alone is insufficient to suppress SF in UFDs.

stars can continuously form down to $z \sim 3$, followed by bursty star formation until $z = 0$. These late time bursts of star formation are unlikely to occur if the simulated massive UFDs were accreted by the MW at early times. In such cases, star formation would be suppressed by environmental factors. This implies that massive UFDs ($M_{\text{vir}} \gtrsim 2 \times 10^9 M_\odot$ at $z = 0$ and $M_{\text{vir}} \sim 2.5 \times 10^8 M_\odot$ at $z = 7$) in the outskirts of the MW are likely to show signatures of late time bursts of star formation. Furthermore, if such massive UFDs are located within the virial radius of the MW, it is expected that, to explain their uniformly quenched SFH, they must have been capture by the MW at early times.

To explore the relative importance of SN feedback, compared to reionization, for the suppression of star formation, we perform a comparison simulation NOSN (see dotted lines in Figure 2). This run is identical to HALO1, except that the thermal SN feedback is excluded, but metals are ejected from stars to model the transition of star formation from Pop III to Pop II. We find that, while reionization plays an important role in inhibiting star formation, SN feedback is crucial for the ultimate quenching of UFDs. Although the UV background is turned on in the same way as before (HALO1), no quenching of star formation is found this time, implying that reionization alone is insufficient to completely suppress star formation in the absence of SN feedback. We should note that

we terminate the run NOSN at $z \sim 2$ for the sake of computational economy.

The bottom right-hand panel of Figure 2 illustrates that all haloes form more than 90% of stars prior to reionization, with the noticeable exception of HALO6. Following Ricotti & Gnedin (2005), our five galaxies can be considered as “true fossils”, as more than 70% of their stars formed before reionization. On the other hand, HALO6 only forms $\sim 30\%$ of stars before reionization and continues to form stars down to $z = 0$, and hence it could be categorized as a “polluted fossil”.

3.2. Residual Gas

Whether or not a halo can form stars at a given time can be illustrated by the maximum gas density, achieved inside the virial radius of the simulated haloes, shown in the upper right-hand panel of Figure 2. In this panel, we compare the maximum hydrogen number density with the adopted density threshold of $n_{\text{H}} = 100 \text{ cm}^{-3}$ (solid horizontal line), above which gas can form stars. We point out that the maximum gas density can get as high as $n_{\text{H}} \sim 10^4 \text{ cm}^{-3}$ at high redshift $z \gtrsim 7$. The final maximum gas density at $z = 0$ is heavily dependent on the specific SFH experienced by a galaxy. For instance, a majority of gas is evacuated both by the UV background and SN feedback in the low mass haloes (HALO1, HALO2, HALO3); hence, little gas has remained, even-

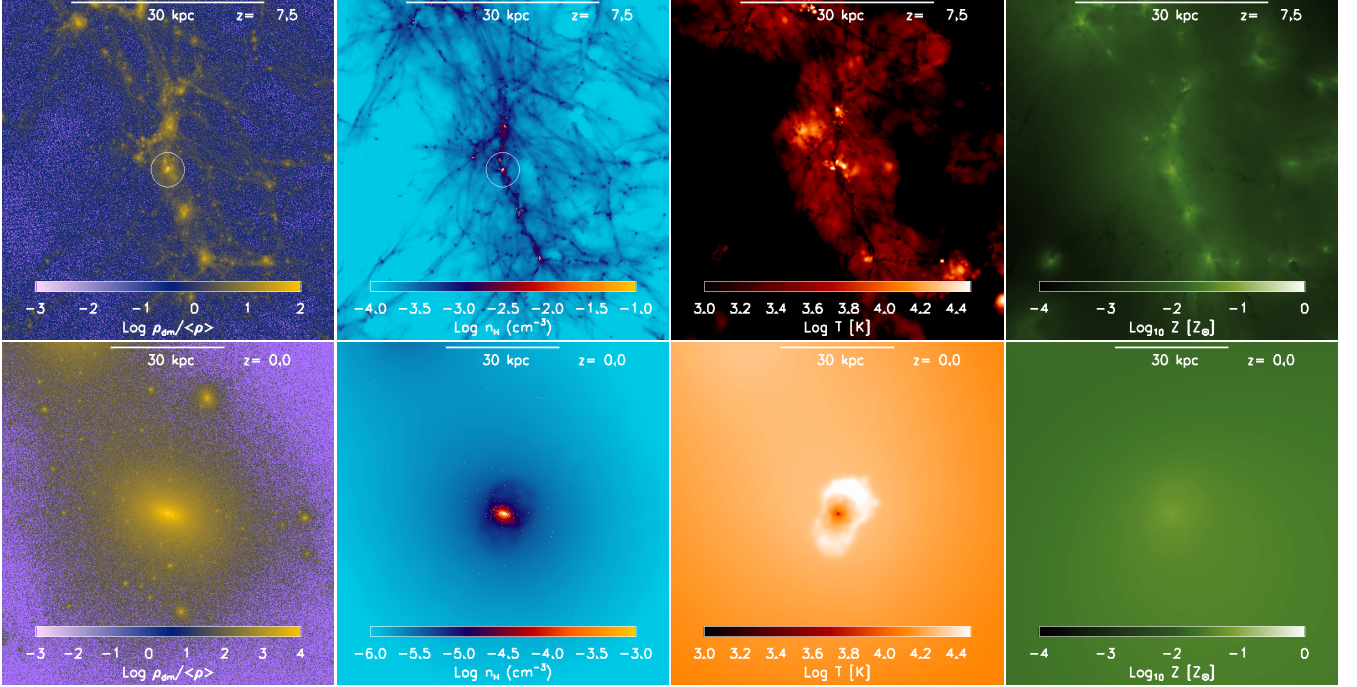


FIG. 3.— Visualization of the zoom-in region, centered on HALO4, at $z = 7.5$ (top panels) and at $z = 0$ (bottom panels), respectively. From left to right: each panel displays dark matter over-density relative to average density in Universe, hydrogen number density, gas temperature, and gas metallicity. The radius of the primary halo, the most massive progenitor at a given time, is denoted as the white circle in the dark matter over-density map (upper left-most panel). At $z = 0$, HALO4 still forms stars, some of which explode as SNe. The gas heated by the SN explosions is clearly shown in the temperature map at $z = 0$. We see that, at $z = 7.5$, stars are formed and explode as SNe within multiple progenitor haloes and they have been assembled into the primary halo. As a result, the galaxy at $z = 0$ is composed of stars, some of which have originated from different haloes, later cannibalized by the primary.

tually resulting in the very low maximum density of $n_H \sim 10^{-5} \text{cm}^{-3}$ at $z = 0$. Even though HALO5 is massive enough to form stars at late epochs, SN feedback from the late starbursts significantly evacuates the gas from the halo, such that the maximum density is as low as $n_H \sim 10^{-4} \text{cm}^{-3}$ at $z = 0$. Meanwhile, we identify high density gas with $n_H \gtrsim 10 \text{cm}^{-3}$ in HALO6 at the end of the simulation. The total residual gas mass of low mass UFDs is $\sim 10^6 M_\odot$ and for the higher mass ones it can be as high as a few by $10^7 M_\odot$. We find that the ionized gas fraction at $z = 0$, defined as gas with a free electron fraction of $f_{\text{elec}} \gtrsim 0.99$, is $\sim 54\%$ in HALO6 and $\sim 74\%$ in HALO4, while the gas is completely ionized in the other haloes.

Figure 3 illustrates the morphology of the refined region, centered on HALO4, at $z = 7.5$ (top panels) and at $z = 0$ (bottom panels), respectively. From left to right, each panel shows dark matter over-density, hydrogen number density, gas temperature, and gas metallicity. At $z = 7.5$, given the distribution of the heated and polluted gas by the SN explosions, stars are formed not only in the main halo, denoted as the white circle at the center of the top panels, but also out of gas in multiple progenitor haloes that eventually have been assembled into the main halo at $z = 0$. Owing to the ongoing star formation at $z = 0$, the gas in HALO4 is significantly heated up to $T \gtrsim 10^5 \text{K}$, as shown in the temperature map. We should emphasize that such late bursts of star formation, triggered by the existence of dense gas, are not shown in the UFDs within the virial radius of the MW, reinforcing the role of the environmental effects on quenching star formation (e.g. Wetzel et al. 2015). Our

results that there is residual gas in the UFD analogs are consistent with results for more massive dwarfs, which are found to be gas rich (e.g., Geha et al. 2012; Bradford et al. 2015; Stierwalt et al. 2015).

3.3. Metal Enrichment

Given that the simulated galaxies have experienced multiple mergers with other haloes over cosmic time, it is expected that a fraction of stars could have formed in different haloes and been accreted later onto the primary halo, i.e. the most massive progenitor at any given time. In order to distinguish the properties of stars formed in-situ in a primary halo, from those of stars formed externally and accreted at later epochs, in Figure 4 we compare the stellar metallicity as a function of formation time. In the top panel, we plot all stars inside the virial radius of HALO1 at $z = 0$, regardless of their formation sites. In the lower panel we compare with stars formed only within the primary halo (in-situ). Note that each symbol (reversed triangle) indicates a single Pop II stellar cluster.

We note that about 75% of stars in HALO1 at $z = 0$ have originated from different progenitor haloes and were assembled into the primary halo at later times via mergers. We can further classify these externally formed stars into two categories: (1) stars formed out of gas that is externally metal-polluted due to the proximity of neighboring haloes hosting SNe; and (2) stars born within a halo that is independently massive enough to form Pop III stars and subsequent generations of stars (in-situ). The latter case is similar to a primary halo, which contains Pop III stars and subsequently formed

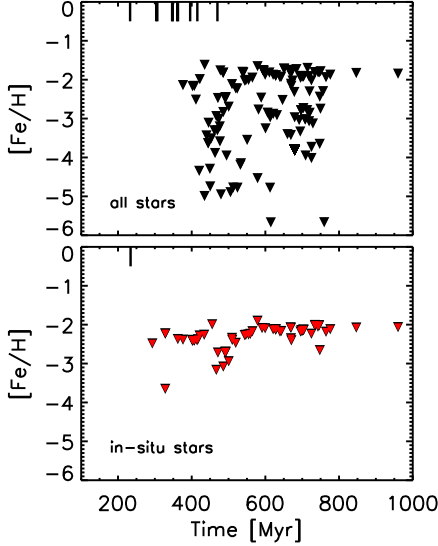


FIG. 4.— Externally vs. internally formed stars. *Top panel:* stellar metallicity vs. formation time for all stars located within the virial radius of HALO1 at $z = 0$. *Bottom panel:* subset of stars formed *in-situ* in the primary progenitor of HALO1. The vertical lines on the top axis mark the formation time of Pop III stars. The absence of low metallicity stars ($[\text{Fe}/\text{H}] \lesssim -3$) among the in-situ sample indicates that low metallicity stars have originated from different progenitor haloes and were assembled into the primary halo at later epochs via mergers. Specifically, such low metallicity stars are polluted via external enrichment, where metals originate in neighboring haloes that host Pop III SNe. This finding is a general feature in all of the simulated analogs.

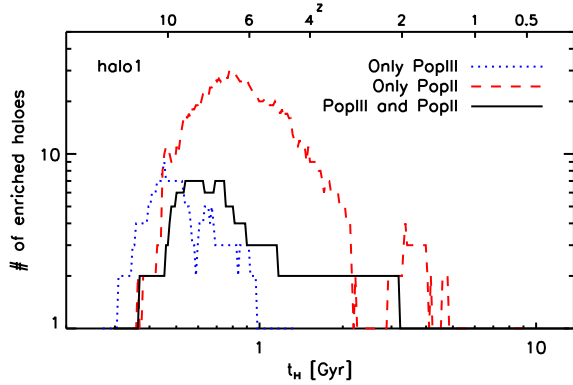


FIG. 5.— Number of haloes that are eventually incorporated into HALO1, divided according to their metal-enrichment path. The blue-dotted line shows the number of haloes that only host Pop III stars or their remnants, while the red-dashed line depicts haloes with only Pop II stars. Finally, the black solid line indicates haloes that host both Pop III and Pop II star formation. The substantial number of Pop II-only haloes (see red dashed line) implies that a large fraction of haloes are externally polluted with metals from neighboring haloes that host SNe. This trend is shown in all of the simulated analogs.

stars via self-enrichment. A striking difference evident in Figure 4 is how broadly stellar metallicity is distributed for all stars, whereas it is concentrated between $[\text{Fe}/\text{H}] = -2$ and $[\text{Fe}/\text{H}] = -3$ for the in-situ sample, except one stellar cluster with $[\text{Fe}/\text{H}] = -3.7$. The absence of low metallicity stars ($[\text{Fe}/\text{H}] \lesssim -3$) among the in-situ sample indicates that low metallicity stars have preferentially come from different progenitor haloes, and later acquired

by the main halo through mergers.

This can be explained as follows. When a Pop III star triggers a SN explosion, the surrounding gas is heated and evacuated from the host halo, locally suppressing further star formation for a certain time period. Detailed studies regarding the duration of this temporary lull in star formation in the wake of a Pop III SN have suggested that it is of the order of a few 10 Myr for a conventional SN energy of 10^{51} ergs. Or, it lasts up to a few hundred Myr for a powerful PISN explosion with 10^{52} ergs, within a host halo of $M_{\text{vir}} \sim 10^5 - 10^6 M_{\odot}$ (e.g. Greif et al. 2009; Ritter et al. 2012; Jeon et al. 2014).

During this period of inhibited star formation, metals are propagated into the ISM and IGM, and can be mixed with pristine gas residing in neighboring minihaloes. If the gas density in such polluted neighboring haloes happens to be high enough to form stars, metal-enriched Pop II stars would be born. Because only small amounts of metals would be delivered to neighboring haloes, the metallicity of the gas that is located in the central region of the externally enriched halo would be low, giving rise to the formation of low metallicity stars. Note that owing to the compactness of the early Universe, the typical distance between minihaloes with $M_{\text{vir}} \sim 10^5 M_{\odot}$ is $\sim 300 - 500$ pc, making it possible to transfer metals to neighboring haloes (Smith et al. 2015).

The bottom panel of Figure 4, on the other hand, implies that the in-situ stars are likely born in an environment that is internally polluted, thus experiencing self-enrichment. The primary progenitor halo forms the first Pop III stars at $t_{\text{H}} \sim 230$ Myr, indicated by the vertical mark on the top axis. The following Pop III SN explosion leads to a suppression of star formation for ~ 50 Myr. Afterwards, the ejected gas is replenished along the cosmic web, and the central gas again reaches densities high enough to form Pop II stars. We find that in a given halo, only one or two Pop II clusters are formed out of gas directly polluted with metals from Pop III SNe, implying that only a few Pop II stars will preserve the intrinsic chemical signatures of Pop III stars (Ji et al. 2015).

In order to estimate how many externally enriched progenitors contribute to the formation of the simulated dwarf galaxy at $z = 0$, we present in Figure 5 the number of haloes with different metal-enrichment paths, that end up in the primary halo (HALO1) through mergers. The red-dashed line indicates the number of haloes that host only Pop II stars without the presence of any Pop III stars or their remnants, implying that they have been externally polluted. The blue-dotted and black-solid lines correspond to haloes hosting Pop III only, or both Pop III and Pop II stars, respectively. The displacement between the blue-dotted and black-solid lines can be understood as the time delay when Pop III star formation transitions to Pop II, in haloes eventually hosting Pop III remnants and Pop II stars. This time delay turns out to be about a few tens of Myr. Interestingly, the number of externally enriched haloes increases up to ~ 30 until $z \sim 6$, as the ISM and IGM are enriched with metals from Pop III and Pop II SNe, but their number declines after reionization, mainly due to the inability of forming stars in low-mass haloes from gas heated by reionization. We point out that as global metal enrichment progresses, no Pop III-only haloes exists ~ 1 Gyr after the big bang. Note that all these findings are general features in all of the simu-

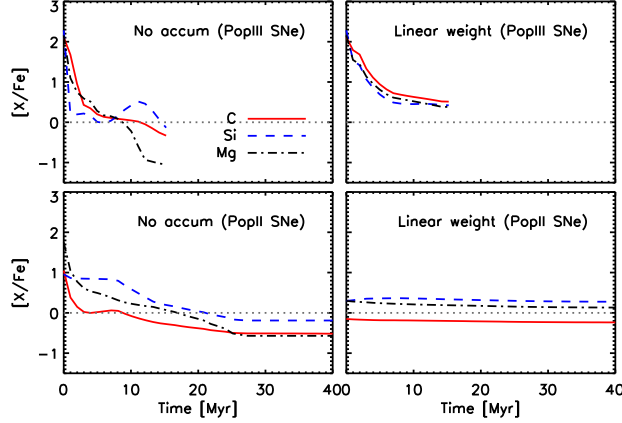


FIG. 6.— Evolution of metal yields of Type II SNe from Pop III (*top panels*) and Pop II stars (*bottom panels*). We assume two cases: (1) metals from individual SN events immediately propagate onwards, and thus do not accumulate in the high density region at the center of a halo (*left*); or (2) their transport is slow, such that metals pile up in the central region, giving rise to an effective yield (*right*). For the former case, subsequently forming stars are sampling the metal yields from the most recent SN only, whereas the latter case means that next-generation stars will be born out of gas polluted with metals from multiple SNe. Note that Pop III yields are displayed only up to ~ 15 Myr, corresponding to the lifetime of a $10 M_{\odot}$ Pop III star, the lowest mass considered in this work. The Pop II yields extend to longer times, in accordance with their lower masses.

lated analogs.

3.4. Chemical Abundances

In this section, we first explain the general trends of the resultant chemical abundances, depending on different stellar populations, Pop III and Pop II. Then, we discuss individual abundances, carbon and alpha-elements based on the expected trends, and finally present metallicity distribution functions and comparisons to results for observed UFDs.

3.4.1. General Trends

To better understand our simulation results, we now introduce a simple toy model for the chemical evolution from multiple SNe. Specifically, in Figure 6 we illustrate the evolution of metal yields, as a function of time since the most massive star has exploded, for a Pop III (*top*) and Pop II (*bottom*) cluster. The panels on the left and right explore different assumptions for the efficiency of metal transport (see below). We only present the Pop III yields up to 15 Myr, which corresponds to the lifetime of the lowest-mass, and thus longest-lived, Pop III star for our chosen IMF, where $m_{*,\text{Pop III}} = 10 M_{\odot}$ (Schaerer 2002). For Pop II, we extend the yields to later times, corresponding to the lower mass progenitor stars present in this case ($m_{*,\text{Pop II}} = 8 M_{\odot}$). In our idealized enrichment model, metals are released in time such that those from the most massive stars are ejected first. Therefore, the gas metallicity at the SN explosion site changes over time, and one of the key factors is how rapidly metals can be transported to large distances. For example, if the timescale for metal transport is shorter than the time between consecutive SNe, then the metallicity of a newly formed star will be determined mostly by SN yields from the most recent event. In this case, metals

from earlier SNe would already have escaped into the surroundings. Conversely, if their propagating timescale is long, the metals ejected from different SNe will linger in the central region of a halo. The metallicity of a newly-formed star would then reflect averaged yields, deposited by multiple SNe.

To further construct our simple model, we consider two extreme cases of how efficiently metals are transported: (1) ejected metals are not accumulated in the central star forming region, and are instead immediately dispersed into the IGM; or (2) a certain fraction of the metals from each SN remains in the central region, thus giving rise to effective yields. The latter are calculated with a linear weight, measuring the time since explosion, such that the most recent SNe contribute most to the average. Or formally, we employ a mass-dependent weight as follows: $w(m_*) = (t - \Delta t(m_*))/t$, where t is the time since the explosion of the most massive star in the cluster, and $\Delta t(m_*)$ is the time since a progenitor with mass m_* exploded. We find that the general trend of the yields from Pop III and Pop II SNe is substantially different. First, Pop III SNe produce more carbon compared to Pop II events. Second, for Pop III yields, the $[\text{C}/\text{Fe}]$ ratio is similar or larger than $[\alpha/\text{Fe}]$, especially $[\text{Mg}/\text{Fe}]$, while these trends are opposite for Pop II yields. These distinctive yield trends thus allow us to distinguish whether stars are formed under the dominant influence of Pop III or Pop II SNe.

We now compare these trends, obtained within the toy model above, with the detailed enrichment results from our full simulations. As discussed above, in-situ stars likely form in environments internally enriched by Pop II SNe, while stars formed through external metal-enrichment are likely to show Pop III signatures. These trends are evident in Figure 7, where we plot the chemical abundances of stars, formed in our simulations, as a function of their formation time (*left*) and their metallicity (*right*). Recall that individual, inversed triangle symbols indicate single Pop II clusters. Except for the very first stellar cluster, the majority of in-situ stars (*bottom panels*) formed under the influence of Pop II SNe, given that $[\text{Si}/\text{Fe}]$ is larger than $[\text{C}/\text{Fe}]$, which is the predicted trend for Pop II SNe. As an exception, the very first stellar cluster was born out of gas enriched by Pop III SNe, indicated by similar $[\text{C}/\text{Fe}]$ and $[\text{Si}/\text{Fe}]$ ratios, consistent with Pop III SN yields. The chemical abundances of all stars, shown in the upper panel of Figure 7, are established by a mixture of two systems: (1) haloes, mainly polluted via internal enrichment, hosting both Pop III and Pop II stars; and (2) externally contaminated haloes. The existence of stellar clusters that exhibit comparable $[\text{C}/\text{Fe}]$ and $[\text{Si}/\text{Fe}]$ ratios implies that their stars are likely formed out of gas mostly enriched by Pop III stars. To the contrary, a lower value of $[\text{C}/\text{Fe}]$ relative to $[\text{Si}/\text{Fe}]$ signals the dominant contribution from Pop II SNe.

3.4.2. Carbon

Figure 8 shows select chemical abundances of Pop II stars within the virial volume of our simulated galaxies at $z = 0$, specifically $[\text{C}/\text{Fe}] - [\text{Fe}/\text{H}]$ and $[\alpha/\text{Fe}] - [\text{Fe}/\text{H}]$ (left and right columns). The color scheme denotes the formation time of stars, where greyish colors correspond to times before $t_{\text{H}} \sim 4$ Gyr and reddish ones to more recent epochs. As we have discussed in the previous sec-

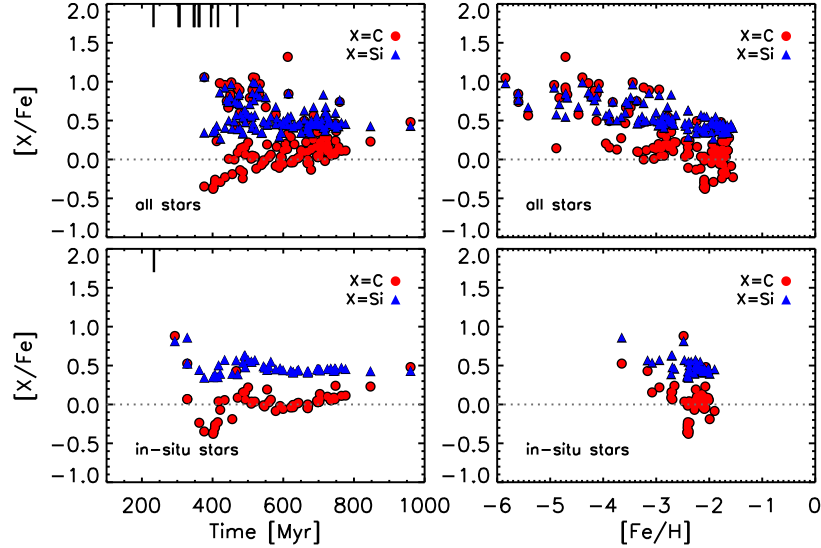


FIG. 7.— Comparison of abundance ratios, $[C/Fe]$ and $[\alpha/Fe]$, of all Pop II stars in HALO1 (*top panels*) versus in-situ stars (*bottom panels*). Following toy model results of Figure 6, we expect that Pop III nucleosynthetic yields show $[\alpha/Fe]$ ratios that are similar to $[C/Fe]$, while $[\alpha/Fe]$ ratios are higher than $[C/Fe]$ in Pop II SN yields. As such, in-situ stars (*bottom*) appear to be predominantly born in environments contaminated by Pop II SNe. Among the *in-situ* stars, only a few stars, formed within a few 10 Myr after the first Pop III SN (*vertical mark on the top axis*), preserve Pop III SN signatures. Low metallicity stars, with $[Fe/H] \lesssim -4$, exhibit the expected trend for Pop III SNe, i.e. comparable $[C/Fe]$ and $[\alpha/Fe]$ ratios, implying that they were formed out of gas enriched by Pop III stars.

tions, star formation in the three haloes, HALO1, HALO2, and HALO3, is truncated close to reionization, and thus *all* their stars form before 1 Gyr, shown as grey-scale colors. The stars in the other three haloes that experience late bursts or continuous star formation span a much wider range of formation times, reflected in the presence of square symbols with reddish colors.

High- and medium-resolution spectroscopic studies of individual member stars in UFDs have revealed that the fraction of carbon-enhanced metal poor (CEMP) stars increases with decreasing metallicities (see Beers & Christlieb 2005 for details; and also, e.g., Aoki et al. 2007; Norris et al. 2013; Yong et al. 2013). Usually, CEMP stars are defined as metal-poor stars with carbon-to-iron ratios above $[C/Fe] = 0.7$ at $[Fe/H] \lesssim -2$ (e.g. Aoki et al. 2007). Several possible mechanisms for their origin have been suggested, including (i) rapidly-rotating massive Pop III stars ($m_* = 40 - 120 M_\odot$), capable of releasing large amounts of CNO-enhanced material (e.g. Meynet et al. 2006), (ii) binary systems with a companion star that undergoes an AGB phase, thus transferring carbon onto a low mass, long-lived, metal-poor star, or (iii) Pop III SNe ($m_* = 10 - 40 M_\odot$) with a low explosion energy. In the latter case, iron-peak elements are more likely to be locked up in the emerging central remnant, whereas those with lower atomic number, such as carbon, are easily ejected. In addition, such ejecta are more likely to rapidly fall back since low SN energies are inefficient to drive the gas out of a host halo (e.g. Umeda & Nomoto 2003; Iwamoto et al. 2005; Cooke & Madau 2014; Salvadori et al. 2015).

Our simulation results indeed exhibit the presence of CEMP stars at low metallicities. Due to the neglect of binary systems, the occurrence of CEMP stars in this work is a consequence of Pop III SNe that intrinsically produce abundant carbon (see, Figure 6). Also, we find that the fraction of CEMP stars is higher at low metal-

licities, $[Fe/H] \lesssim -4$, such that this fraction declines from $> 45\%$ at $[Fe/H] \lesssim -4$ to $< 20\%$ at $[Fe/H] \lesssim -2$ for all haloes. As demonstrated in the right-hand panels of Figure 7, low metallicity, $[Fe/H] \lesssim -3$, stars with high carbon-ratios of $[C/Fe] > 0.7$ originate from Pop III SNe, characterized by their large intrinsic carbon production. As can also be seen, the $[C/Fe]$ ratio decreases toward near-solar values, giving rise to C-normal stars, with increasing metallicity. This behavior is expected as a consequence of self-enrichment by Pop II stars, where carbon yields are normal and the overall gas metallicity rises in the process.

We now compare our simulated abundances with the empirical record in select UFDs. For instance, the member stars of Segue 1 roughly trace the trend of increasing number of CEMP stars toward lower metallicity, except one star with $[C/Fe] = 1.4$ at $[Fe/H] = -1.6$. Based on its enhanced abundance of neutron-capture elements, Frebel et al. (2014) suggest that this outlier star might be associated with a binary system where carbon is transferred from a companion. On the other hand, high-resolution spectroscopy shows that stars in Bootes I both include CEMP signatures at low metallicities, ($[Fe/H] < -3.0$, and C-normal ones at $[Fe/H] \gtrsim -3$ (e.g. Gilmore et al. 2013; Ishigaki et al. 2014; Frebel et al. 2016). Given the co-existence of CEMP and C-normal stars, Bootes I thus appears to be very similar to our simulated galaxies, in particular HALO3, where both classes of stars are naturally produced through a combination of Pop III SNe and self-enrichment by Pop II stars.

3.4.3. Alpha Elements

The run of $[\alpha/Fe]$ over $[Fe/H]$ serves as a well-known cosmic clock, encoding the timescale over which stars have formed. In particular, the existence of a knee, where $[\alpha/Fe]$ begins to decline, has been suggested as a reflec-

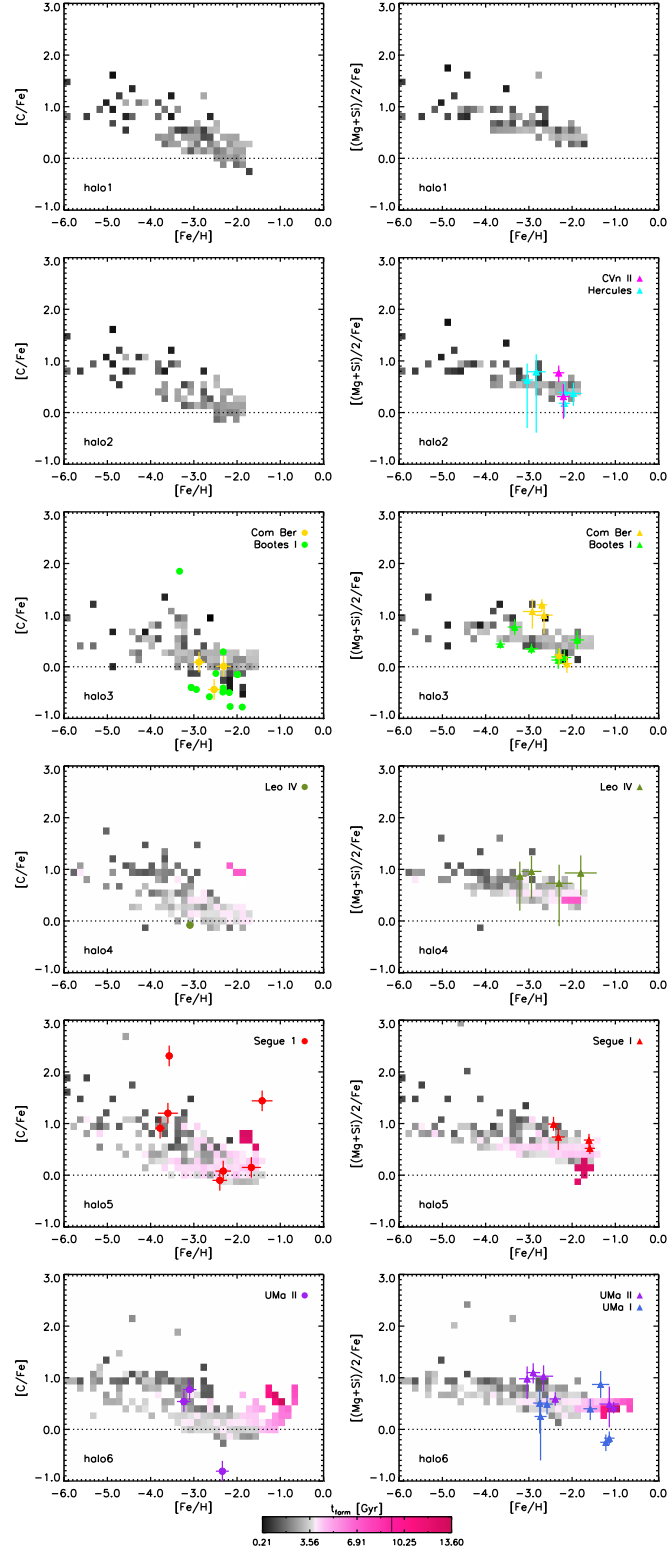


FIG. 8.— Stellar abundances in the simulated galaxies at $z = 0$. *Left column*: $[C/Fe]$ vs. $[Fe/H]$. *Right column*: $[\alpha/Fe]$ vs. $[Fe/H]$. The square symbols denote simulated abundances, with color indicating the formation time of stars, such that grey colors mark stars formed before $t_H \sim 4$ Gyr, and reddish colors those formed after $t_H \sim 4$ Gyr. The existence of CEMP stars, particularly at low metallicities, $[Fe/H] \lesssim -3$, is a consequence of Pop III SNe that intrinsically produce large amounts of carbon. The enhanced α -elements and the absence of clear knees, at which $[\alpha/Fe]$ ratios decline, indicate that the gas in the galaxies is preferentially metal-enriched by Type II SNe, rather than Type Ia, from Pop III and massive Pop II stars. In the most massive HALO6 (*bottom panels*), the gas is metal-enriched up to $[Fe/H] \sim -0.6$, owing to its extended star formation history. Observational data of stellar abundances in select LG UFDs are displayed with the symbols, as labelled in the legends. For carbon, the data is taken from Simon et al. (2010) for Leo I, Frebel et al. (2010) for UMa II and Com Ber, and Frebel et al. (2014) for Segue 1. For Bootes I, the data is from Frebel et al. (2016), who provide a list of all high-resolution measurements from the literature. For the alpha-elements, we use the data given by Frebel et al. (2010) and Gilmore et al. (2013). A detailed comparison between the simulated UFD analogs and the observed UFDs is discussed in Section 3.5.

tion of a long duration of star formation. Given sufficient time, Type Ia SNe would begin to contribute, producing more iron compared to alpha elements. As is evident in the right panels of Figure 8, we see roughly flat $[\alpha/\text{Fe}]$ abundances at low metallicities, $[\text{Fe}/\text{H}] \lesssim -3$, in all runs. As discussed in the previous sections, such low metallicity stars are likely to be formed via external metal enrichment by Pop III SNe. We note that relatively massive haloes, HALO4, HALO5, and HALO6, show considerable scatter in the α -abundance ratio, including values as high as $[\alpha/\text{Fe}] \gtrsim 2$. This scatter can be understood as follows. The number of progenitor haloes, hosting Pop III stars, rises with increasing halo mass. As a result, the gas is incorporated from multiple haloes that are contaminated by different Pop III SNe at a given time, leading to a large spread in $[\alpha/\text{Fe}]$ ratio (see, Figure 6). We should mention that our simulations can only trace a few alpha elements, including Si and Mg, limiting our ability to compare to observations.

Among the simulations, the less massive haloes, HALO1, HALO2, and HALO3, exhibit enhanced $[\alpha/\text{Fe}]$ ratios over the entire metallicity range, extending to $[\text{Fe}/\text{H}] \sim -2$, without an obvious decline at high $[\text{Fe}/\text{H}]$. The absence of a distinct knee implies that the stars in these haloes have formed out of gas that was preferentially polluted with metals from Type II rather than Type Ia SNe. In contrast, the most massive systems, HALO5 and HALO6, show hints of Type Ia SNe. For instance, stars formed late in HALO5 at $z \sim 0.5$ (see Figure 2) have near- or super-solar $[\alpha/\text{Fe}]$ ratios at $[\text{Fe}/\text{H}] \sim -1.6$. Unlike the other haloes, owing to the extended star formation, stellar metallicity in HALO6 increases extending to $[\text{Fe}/\text{H}] \sim -0.6$. It should be noted that the $[\alpha/\text{Fe}]$ ratio at $[\text{Fe}/\text{H}] \gtrsim -2$ is below that at lower metallicities, but $[\alpha/\text{Fe}]$ still remains super-solar. This is due to the continuous star formation, followed by Type II SNe, which are likely to wash out the impact of Type Ia SNe, by continuously producing abundant alpha elements.

As a limiting case, Frebel & Bromm (2012) proposed a “one-shot enrichment” scenario, where feedback from massive Pop II stars, themselves showing pure Pop III chemical signatures, evacuated the remaining gas from their host halo, thus completely suppressing further star formation until $z = 0$. Thus, any long-lived Pop II stars in these systems would exhibit a constant alpha-element ratio, $[\alpha/\text{Fe}] = 0.35$, which is solely determined by the yields of Pop III Type II SNe. This should be, however, considered an extreme case, valid for small, isolated haloes, not undergoing continued accretion or mergers. Thus, our simulated galaxies are not the case in which a halo grows in mass, making the gas in the halo with a deepened potential well harder to escape, rendering the effectiveness of stellar feedback weaker. Furthermore, the evacuated gas will begin to fall back within the order of a few 10 Myr, triggering subsequent episodes of star formation (e.g. Ritter et al. 2012; Jeon et al. 2014). This multi-generational star formation is reflected as scatter in the $[\alpha/\text{Fe}]$ ratios of observed LG dwarfs.

Measurements of α -elements in MW UFDs are provided by several studies including Vargas et al. (2013), where individual alpha abundance ratios are presented for 61 red giant branch stars in 8 UFDs. They found that all UFDs are likely to show high $[\alpha/\text{Fe}]$ ratio at low

$[\text{Fe}/\text{H}] < -2.5$, which is consistent with the results of our simulations. In particular, Segue 1 and UMa II exhibit enhanced alpha-abundances across the observed metallicity range $-3.5 < [\text{Fe}/\text{H}] < -1.0$, indicative of the signature of Type II SNe, while the other six systems show a general trend of decreasing $[\alpha/\text{Fe}]$ ratio with increasing $[\text{Fe}/\text{H}]$. However, none of the observed UFDs has yet revealed $[\alpha/\text{Fe}]$ ratios below $[\text{Fe}/\text{H}] \sim -3.5$, preventing us from comparing our predictions on extremely low-metallicity stars with observations.

Overall, our predictions for the $[\alpha/\text{Fe}]$ ratio show good agreement with observations over the metallicity range $-3.5 < [\text{Fe}/\text{H}] < -1.0$. The observations also show that most UFDs exhibit no clear knee, favoring the interpretation that their stars were born out of gas dominantly polluted by Type II SNe (e.g. Vargas et al. 2013; Gilmore et al. 2013). To be specific, the measured $[\alpha/\text{Fe}]$ ratios of CVn II and Hercules are consistent with those of HALO2, while the values of Coma Berenices and Bootes I agree with those of HALO3. These are relatively less massive haloes, $M_{\text{vir}} \lesssim 3 \times 10^9 M_{\odot}$, experiencing truncated star formation. Furthermore, HALO4 and HALO5 show excellent agreement with Leo IV and Segue 1, in combination with their measured $[\text{C}/\text{Fe}]$ ratios and the observed maximum metallicity.

3.4.4. Metallicity Distribution Function

In Figure 9, we display normalized stellar metallicity distribution functions (MDFs) for the simulated galaxies, i.e., the fraction of Pop II stars as a function of $[\text{Fe}/\text{H}]$, in order of decreasing stellar mass, beginning from the top-left panel. The general shape of the MDF exhibits a peak that gradually declines toward the low-metallicity regime, and sharply drops above the peak. The location of the peak shifts from $[\text{Fe}/\text{H}] \sim -1$ for the most massive halo HALO6, with a stellar mass of $M_{\star} \sim 8.8 \times 10^5 M_{\odot}$, to $[\text{Fe}/\text{H}] \sim -2$ for HALO2, where $M_{\star} \sim 3.8 \times 10^4 M_{\odot}$. Our derived MDFs reflect the combined action of external metal-enrichment by Pop III and self-enrichment by Pop II stars. Since the low-metallicity stars have predominantly originated in haloes affected by Pop III SNe, the resultant fraction is expected to be small due to the brief Pop III era, thus giving rise to the extended tails. The self-enrichment by Pop II stars, on the other hand, increases the gas metallicity in their host halo, imprinting the peak at high $[\text{Fe}/\text{H}]$.

We also plot observed MDFs for select UFDs, shown as dotted lines, provided by Brown et al. (2014). Our simulations can approximately reproduce the range of metallicity, especially the upper limit, for Leo IV and Bootes I, but fail to simultaneously account for the peak of the observed MDFs. We find that none of the MDFs of the observed UFDs is matched with the MDF of HALO6 that reflects the prolonged star formation down to $z = 0$, resulting in the peak at the relatively high metallicity ($[\text{Fe}/\text{H}] \gtrsim -1$) via self-enrichment. This discrepancy supports the assertion that the environmental effects within the virial radius of the MW are responsible for the truncated star formation in the relatively massive UFDs at late time, providing a constraint on the accretion epoch of UFDs. However, we should emphasize that the empirical record, in particular for low metallicity stars, is currently still very much subject to small-number statistics, such that definitive conclusions

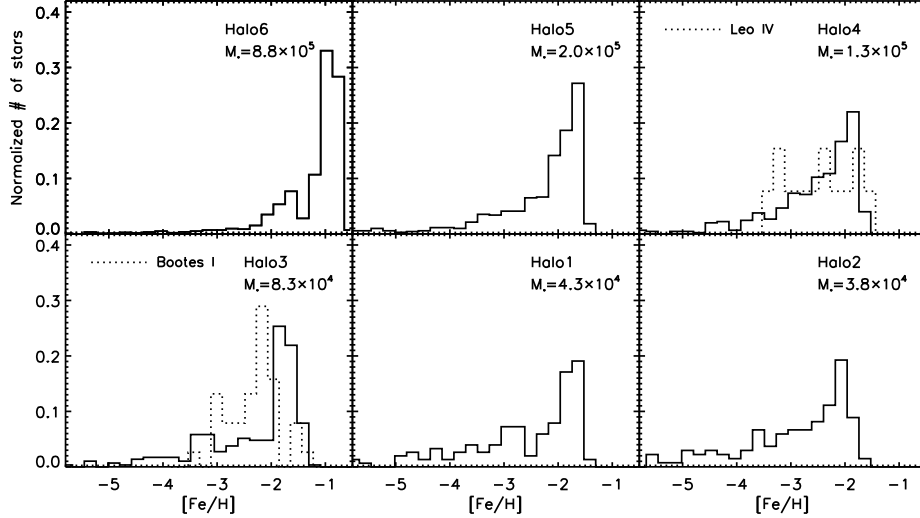


FIG. 9.— Normalized metallicity distribution function (MDF) of Pop II stars for each halo, ordered according to decreasing stellar mass (beginning in the upper-left panel). The MDF of haloes with stellar mass larger than $M_* > 10^4 M_\odot$ shows a peak at $[\text{Fe}/\text{H}] \sim -2$, below which it gradually declines toward the low-metallicity regime. Such MDF shape is a natural consequence of both Pop III and Pop II SNe contributing: the peak at $[\text{Fe}/\text{H}] \sim -2$ is due to the continuing self-enrichment by Pop II stars, whereas the low-metallicity tails represent stars formed in neighboring haloes under the influence of Pop III SNe. As a result, such low-metallicity stars are likely to preserve the signatures of Pop III SNe. Owing to the prolonged SFH of HALO6, the MDF peaks at $[\text{Fe}/\text{H}] \sim -1$, but none of the observed UFDs can explain such distribution, implying that environmental effects within the virial radius of the MW would play a critical role in terminating star formation in relatively massive UFDs. Otherwise, they would have continuously formed stars in the field.

cannot be reached yet.

3.5. Connection to the Observed UFDs.

In this section, we attempt to provide insight into the quenching and accretion timescales of the observed UFDs around the MW based on their similarities to our simulated UFD analogs. To be specific, we match the simulated UFD analogs with the observed LG UFDs by comparing the chemical properties, such as $[\alpha/\text{Fe}]$, $[\text{C}/\text{Fe}]$, and $[\text{Fe}/\text{H}]_{\text{max}}$ which is the maximum metallicity. A summary of this comparison is listed in Table 2. For $[\text{Fe}/\text{H}]$ values, we only compare stars with metallicity higher than $[\text{Fe}/\text{H}] \sim -3.5$, below which the observation could be incomplete due to the lack of ability of observing metal-poor stars with current observations.

As shown in Figure 8, we find that the maximum metallicities of the simulated galaxies, $[\text{Fe}/\text{H}]_{\text{max}} \sim -1.8$ (HALO2) and $[\text{Fe}/\text{H}]_{\text{max}} \sim -1.5$ (HALO3), are likely to be consistent with the most metal-rich stars among the observed UFDs, such as CVn II, Leo IV, Coma Berenices, Bootes I, and Hercules. The absence of high metallicity stars above $[\text{Fe}/\text{H}] \sim -1.5$ in such UFDs, in combination with the enhanced $[\alpha/\text{Fe}]$ ratios, could imply that these UFDs might have experienced similar SFHs of the two galaxies, HALO2, and HALO3, that show the early quenching of star formation by reionization. This interpretation is in line with that of Brown et al. (2014), where they report that five UFDs, CVn II, Leo IV, Bootes I, Hercules, and CVn II, show early truncated star formation based on the old ages of their stellar populations, finding that 80% of their stars formed prior to $z = 6$. Here, we have demonstrated for the first time that the theoretically expected chemical evolution of UFD analogs formed in a cosmological framework are consistent with this early truncation of star formation.

In addition to the excellent agreement of $[\alpha/\text{Fe}]$ ra-

tios of Bootes I with those of HALO3, the co-existence of CEMP and C-normal stars can be reproduced in HALO3, in which CEMPs are likely to be formed via Pop III SNe, while C-normal stars are a consequence of self-enrichment by Pop II stars. On the other hand, Segue 1 appears to be similar to HALO4, providing good agreement between the observed and simulated chemical properties such as $[\text{Fe}/\text{H}]_{\text{max}} \sim -1.42$, $[\text{C}/\text{Fe}]$, and $[\alpha/\text{Fe}]$. As pointed out in Section 3.4.2, the star with $[\text{C}/\text{Fe}] = 1.4$ at $[\text{Fe}/\text{H}] = -1.6$ might originate from a binary system (Frebel et al. 2014). Therefore, we could ignore this outlier since binary systems are not considered in this work. We find that HALO4 exhibits bursty star formation at late epochs at $z \sim 3.9$, during which time stars are formed with relatively high metallicities ($[\text{Fe}/\text{H}] \sim -1.6$). This suggests that star formation in Segue 1 might be not completely truncated by reionization, but followed by late bursts of star formation that gives rise to stars with $[\text{Fe}/\text{H}] \gtrsim -1.6$. We find that none of the simulated UFD analogs exhibit similar chemical properties of UMa I.

These simulations can thus be used to predict the SFH for a given UFD, based on its observed chemical properties. For example, the $[\alpha/\text{Fe}]$ ratios of UMa II are consistent with the derived $[\alpha/\text{Fe}]$ ratios of HALO6, which is a halo that shows extended star formation beyond reionization. However, HALO6 fails to match $[\text{Fe}/\text{H}]_{\text{max}} = -1.04$ of UMa II (Gilmore et al. 2013), by producing stars with metallicity higher than $[\text{Fe}/\text{H}] \sim -1.04$. This discrepancy might indicate that reionization was insufficient to completely suppress star formation in UMa II, allowing it to continuously form stars after reionization, but afterwards it is clear that star formation was truncated by other factors, i.e., gas stripping during the infall into the MW halo. The simulations suggest that without this truncation UMa II might have continuously or

TABLE 2
SUMMARY OF COMPARISON BETWEEN THE SIMULATED
UFD ANALOGS AND THE OBSERVED UFDs.

UFDs	$M_* [M_\odot]$	Analog	Similar properties
Segue I	1.0×10^3	HALO5	$[\alpha/\text{Fe}]$, $[\text{C}/\text{Fe}]$, $[\text{Fe}/\text{H}]_{\text{max}}$
Com Ber	3.7×10^3	HALO3	$[\alpha/\text{Fe}]$, $[\text{C}/\text{Fe}]$
UMa II	4.1×10^3	HALO6	$[\alpha/\text{Fe}]$, $[\text{Fe}/\text{H}]_{\text{max}}$
CVn II	7.9×10^3	HALO2	$[\alpha/\text{Fe}]$
Leo IV	1.0×10^4	HALO4	$[\alpha/\text{Fe}]$, $[\text{C}/\text{Fe}]$, $[\text{Fe}/\text{H}]_{\text{max}}$
UMa I	1.4×10^4	NONE	-
Bootes I	2.9×10^4	HALO3	$[\alpha/\text{Fe}]$, $[\text{C}/\text{Fe}]$, $[\text{Fe}/\text{H}]_{\text{max}}$
Hercules	3.7×10^4	HALO2	$[\alpha/\text{Fe}]$, $[\text{C}/\text{Fe}]$, $[\text{Fe}/\text{H}]_{\text{max}}$

NOTE. — Column (1): the names of the observed UFDs. Column (2): stellar mass in M_\odot . Column (3): the name of the most similar analogs among the simulated galaxies based on the chemical properties listed in Column 4.

episodically formed stars down to $z = 0$, producing stars with metallicity above $[\text{Fe}/\text{H}] \sim -1.04$, as predicted in HALO6.

If we assume that the end of star formation of UMa II is instead correlated with the infall time into the MW halo, the simulated analog, HALO6, allows us to estimate the infall time of UMa II. In Figure 10, we present the evolution of chemical abundances of HALO6, $[\alpha/\text{Fe}]$ vs. $[\text{Fe}/\text{H}]$, at different redshifts, $z = 7$ (top), $z = 6$ (middle), and $z = 3$ (bottom), with those of UMa II at $z = 0$. As shown in the middle panel of Figure 10, the larger value of $[\text{Fe}/\text{H}]_{\text{max}} \sim -1.04$ of the most metal-rich stars in UMa II, compared to that of HALO6, indicates an incapability of complete quenching of star formation by reionization. As stars in HALO6 are continuously formed, the metallicity increases, eventually forming stars with metallicity as high as $[\text{Fe}/\text{H}] \sim -1.04$ at $z \sim 3$. Provided that there are no observed stars with metallicity higher than $[\text{Fe}/\text{H}] \sim -1.04$ in UMa II, our simulations indicate that its SFH was truncated at $z \sim 3$.

If we assume that the infall onto the MW was responsible for the quenching of star formation in UMa II, we can estimate that UMa II fell in ~ 11 Gyr ago. This prediction is consistent with the results of Rocha et al. (2012), where they investigate the infall times for MW dwarfs using their present-day kinematics and the energy-infall relation. They suggest that UMa II tends to support an early infall with $t_{\text{infall}} \sim 8 - 11$ Gyr.

We note that it is impossible to infer the accurate infall times of the observed UFDs from this work, since the simulated galaxies are in the field, which is beyond the virial radius of the MW-like host halo. However, these simulations illustrate that the absence of stars with $[\text{Fe}/\text{H}] > -1.04$ in a given UFD strongly indicates that its SFH is truncated prior to $z = 3$.

3.6. Global Galaxy Properties

We present global galaxy properties at $z = 0$ inferred from the simulations in Figure 11. The relationship between stellar and halo mass of galaxies is shown in the top panel, where the red filled circles denote our simulations. Results from other works are also displayed, including hydrodynamic simulations (e.g. Simpson et al.

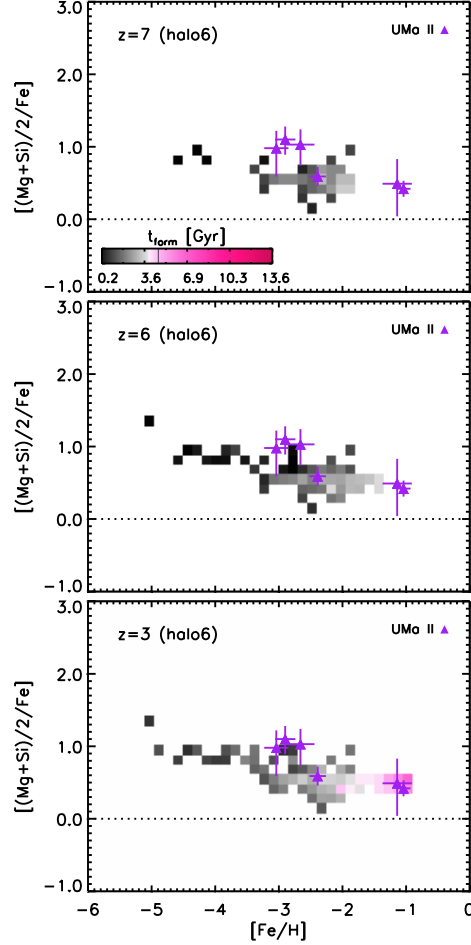


FIG. 10.— The evolution of stellar abundances, $[\alpha/\text{Fe}]$ vs. $[\text{Fe}/\text{H}]$, in HALO 6 at different redshifts, $z = 7$ (Top), $z = 6$ (Middle), and $z = 3$ (Bottom), by comparing with the observed values of UMa II at $z = 0$ (Gilmore et al. 2013). As demonstrated in the middle panel, the discrepancy in $[\text{Fe}/\text{H}]_{\text{max}} \sim -1.04$ between HALO6 and UMa II indicates that reionization was insufficient to completely quench star formation in UMa II. HALO6 forms stars with such metallicities at $z = 3$ (bottom panel), meaning that UMa II formed stars down to $z = 3$ and truncated afterwards. Furthermore, if we assume that the end of star formation of UMa II is correlated with gas stripping while falling onto the MW halo, then the HALO6 results suggest an estimated infall time for UMa II that is as old as ~ 11 Gyr ago.

2013; Munshi et al. 2013; Shen et al. 2014; Oñorbe et al. 2015; Wheeler et al. 2015), and abundance matching using dark-matter simulations (e.g. Behroozi et al. 2013; Brook et al. 2014; Garrison-Kimmel et al. 2016). Given that our spatial and mass resolutions are comparable to Wheeler et al. (2015) and Oñorbe et al. (2015), the discrepancy in the predicted stellar masses might be attributed to additional feedback effects considered there. Specifically, they also take into account the impact of photoheating and radiation pressure from stars, which could reduce star formation.

Our results show good agreement with a fit, $M_* \propto M_{\text{vir}}^{1.8}$, suggested by Garrison-Kimmel et al. (2016), who derived the relation based on LG galaxy counts and the results of dark-matter simulations. The average stellar metallicity vs. V-band luminosity is presented in the

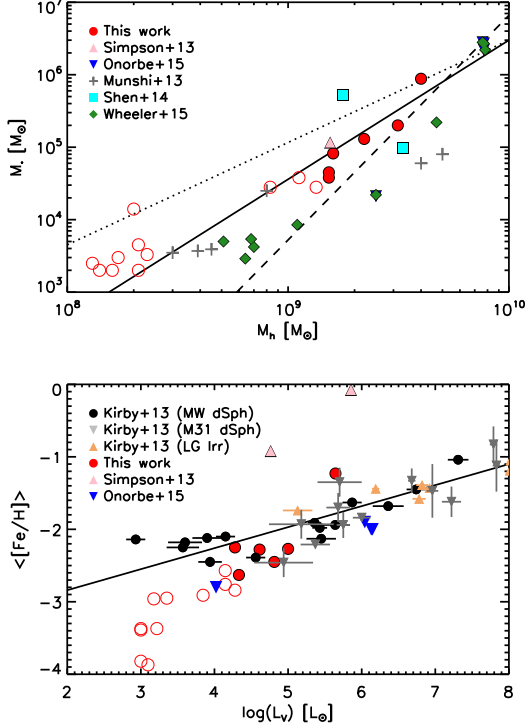


FIG. 11.— Global physical properties of the simulated dwarf galaxies at $z = 0$, stellar mass vs. halo mass (*top*) and stellar metallicity vs. luminosity (*bottom*). The quantities derived from our work are shown as red filled circles. We also show results from other hydrodynamic simulations (Simpson et al. 2013; Munshi et al. 2013; Shen et al. 2014; Wheeler et al. 2015; and Onorbe et al. 2015), as well as select observations (Kirby et al. 2013). In the top panel, we compare our stellar-halo mass results to theoretical fits from abundance matching techniques (Behroozi et al. 2013 (dotted line), Brook et al. 2014 (dashed line), and Garrison-Kimmel et al. 2016 (solid line)); as can be seen, our results show good agreement with the fit suggested by Garrison-Kimmel et al. (2016). We also mark the properties of low-mass galaxies ($M_{\text{halo}} < 10^9 M_\odot$, red open circles) that are located around the six galaxies (HALO1-HALO6). These galaxies are composed of only a small number of stellar clusters formed via external metal-enrichment, giving rise to low average metallicity.

bottom panel of Figure 11, and compared again with other works and observations. The V-band luminosity is computed by assuming a stellar mass-to-light ratio of $2 M_\odot / L_\odot$ for an old stellar population (Kruijssen & Mieske 2009). The average stellar metallicity ranges from $[\text{Fe}/\text{H}] = -1.23$ for a few $5 \times 10^5 L_\odot$ galaxy to $[\text{Fe}/\text{H}] = -2.63$ for $2 \times 10^4 L_\odot$ systems, which is in good agreement with observations.

In addition to the six haloes (HALO1-HALO6), we also present the properties of small galaxies ($M_{\text{halo}} < 10^9 M_\odot$, red open circles) around the six haloes in the refined regions. A noticeable discrepancy from the observed relation is that such small galaxies result in much smaller stellar metallicity, by an order of magnitude, at luminosities below $L_V \sim 10^{3.5} L_\odot$. This corresponds to systems in which only a few stars are formed by external metal enrichment, and where subsequent star formation is self-terminated by SN feedback, evacuating all remaining gas. Afterwards, these systems are unable to replenish their gas supply, owing to their shallow potential well. As a result, those low-mass galaxies are composed

of only a small number of stellar clusters that form in externally-enriched environments, giving rise to low average metallicity. However, the robustness of the derived properties of such small galaxies is subject to mass resolution. Therefore, we plan to firm up this possible external enrichment pathway with even higher-resolution simulations in future work.

4. CAVEATS AND LIMITATIONS

In this section, we briefly comment on the limitations of this work and our adopted assumptions that could affect the results. One of the robust results of our work is the key role of external metal enrichment in the formation of extremely metal-poor stars. The degree of external metal enrichment, however, heavily depends on how we implement the transport of metals and their mixing with the surrounding gas. In the diffusion method, adopted here, the efficiency of mixing is determined by the diffusion coefficient described in Section 2.4.3.

To test the robustness of our results regarding the efficiency of metal mixing, we additionally perform a comparison simulation. Here, we artificially reduce the diffusion coefficient by a factor of 5 in the HALO1 zoom-simulation, and examine if we still can produce extremely low metallicity stars. We find that the fraction of stars, defined as $f = (\text{number of stars with metallicity less than a given } [\text{Fe}/\text{H}]) / (\text{total number of stars})$, decreases for $f([\text{Fe}/\text{H}] < -3)$, $f([\text{Fe}/\text{H}] < -4)$, and $f([\text{Fe}/\text{H}] < -5)$ by a factor of 1.5, 1.2, 1.04, respectively. Given the stochastic nature of star formation, we conclude that the ability of producing low-metallicity stars within our simulations is not very sensitive to changes in the diffusion coefficient. We note that external metal-enrichment is argued to be much less important in the recent work by Griffen et al. (2016), where they investigate the fossils of Pop III star formation and of the first galaxies in a MW-mass system. The idealized model for metal pollution, implemented in post-processing within their dark-matter only simulation, however, makes it difficult to directly compare with their results.

Other uncertainty that could affect the resulting chemical abundances would be the IMF of Pop III and Pop II stars. As previously mentioned, the Pop III IMF, in particular, is still very uncertain. Here, we only consider the mass range between $10 M_\odot$ and $150 M_\odot$ by assuming a top-heavy IMF, but recent high-resolution studies of Pop III star formation have suggested that the mass of primordial stars could extend to as low as $m_* < 1 M_\odot$ (e.g. Stacy et al. 2016). If this were the case, our simulations would have overproduced metals, and overpredicted alpha-element abundances as well, via CCSNe and PISNe from massive Pop III stars.

We do not take into account photoheating and radiation pressure from stars. For the low-mass galaxies simulated here, these additional stellar feedback effects may play an important role in suppressing star formation. In this context, Wise et al. (2012) have reported that the star formation rate can be reduced by a factor of five in a dwarf galaxy at $z \sim 8$ with a virial mass of $2 \times 10^8 M_\odot$ by including radiation pressure. Similarly, the key role of radiative feedback in predicting the stellar masses of galaxies, in particular at high redshifts, is emphasized in the study by Hopkins et al. (2014). However, it is currently still prohibitive computationally to trace the

evolution of a galaxy down to $z = 0$, while directly solving the radiative transfer equation for our highly resolved star forming regions within their large-scale cosmological context.

It should also be pointed out that we fix the onset of reionization by introducing an external UV background at $z = 7$, ramping it up to its full strength by $z = 6$. Simpson et al. (2013), on the other hand, have shown that depending on the onset of reionization, the resultant stellar mass at $z = 0$ can vary by a factor of 2 (see also Milosavljević & Bromm 2014). The precise time when a given galaxy is impacted by the UV background would depend on how far the galaxy is located from massive haloes, where the majority of UV photons is emitted, implying that dwarf galaxies close to a massive system might experience an early truncation of star formation. In addition, apart from the uniform UV background, local heating and ionization from the nearby galaxy are neglected. The effect of local radiation sources and the impact of the MW potential will be presented in a subsequent paper.

The final point is that the size of our simulation box is relatively small, dictated by the need to keep computational cost under control. We cannot, therefore, properly represent the large-scale modes in the cosmological density field that would control the number of structures at $z = 0$, and would also affect the accretion history of the simulated haloes. However, in this work, we focus on the evolution of individual systems rather than the statistics of sub-structures of a realistic MW-size halo. In addition, performing simulations for multiple refined regions allows us to investigate the build-up of galaxies under different accretion histories, thus partially addressing the impact of cosmic variance.

5. SUMMARY AND CONCLUSIONS

We have performed a suite of cosmological hydrodynamic zoom-in simulations to investigate the star formation history and chemical evolution of local dwarf galaxies. We have, for the first time, traced the detailed enrichment history of stellar populations in local dwarf galaxies, reaching back to the formation of Pop III stars. Our work, therefore, allows us to directly compare the derived stellar chemical abundances, including the contribution from the first stars, to the detailed observations of individual stellar abundances in UFDs. Given the physical characteristics of the local UFDs, which consist of metal-poor, ancient stellar populations ($\gtrsim 10$ Gyr), there have been theoretical attempts to link the nearby UFDs to galaxies at high redshifts ($z \gtrsim 6$). In particular, the truncated star formation history of UFDs, inferred from observations, supports the idea that their star formation could be partially or completely quenched by reionization. The gas in dwarf galaxies was then photo-heated, and the filtering (Jeans) mass in the reionized IGM was increased, such that gas collapse into low-mass haloes became inefficient.

Our simulations confirm that reionization, in combination with supernova feedback, did play a critical role in suppressing star formation in local dwarf galaxies. The effectiveness of reionization in preventing star formation strongly depends on halo mass: star formation in low-mass haloes, with $M_{\text{vir}} \lesssim 2 \times 10^9 M_{\odot}$, is almost entirely quenched by reionization, while relatively massive haloes,

$M_{\text{vir}} \gtrsim 3 \times 10^9 M_{\odot}$, exhibit a continuous or bursty star formation history at late epochs. Our results might imply a crucial role of environmental effects of the MW on quenching star formation in the UFDs that are massive enough not to be entirely truncated by reionization. We find that in most cases, more than 90% of stars form prior to reionization, such that these systems can be classified as “true fossils”. On the other hand, the most massive halo, with $M_{\text{vir}} \sim 4 \times 10^9 M_{\odot}$, forms only about 30% of stars before reionization, and star formation is not effectively shut down. Such a galaxy would correspond to a “polluted fossil”. The comparison run without SN feedback confirms that this feedback is essential in truncating star formation in dwarf galaxies.

Our simulations demonstrate that the inclusion of Pop III SNe is a necessary ingredient to produce low metallicity stars with $[\text{Fe}/\text{H}] \lesssim -4$. Particularly, we find that the existence of such low-metallicity stars is predominantly a consequence of external metal enrichment by Pop III SNe. Due to the proximity between haloes at high redshifts, $z \gtrsim 7$, metals from Pop III SNe can be transferred into neighboring haloes that have never formed stars, but are about to do so. As a result, extremely low-metallicity Pop II stars are likely to be born in this externally contaminated environment. Based on the distinctive trends of metal yields from Pop III and Pop II SNe, we scrutinize the detailed origin of the stellar components in the dwarfs. We show that the simulated galaxies are composite systems, assembled from haloes that were externally enriched, hosting only Pop II stars, and from haloes in which the gas was polluted via self-enrichment, hosting both Pop III and Pop II star formation. Our simulations naturally reproduce the carbon-enhanced metal poor stars by including Pop III SNe that intrinsically yield high ratios of $[\text{C}/\text{Fe}]$. Also, the resultant chemical abundances provide a good match to the observations, in that we find the enhanced $[\alpha/\text{Fe}]$ ratios at all metallicities, a trend also found in the observations of UFDs. This enhanced $[\alpha/\text{Fe}]$ ratio, nearly constant with metallicity, implies that the gas in the dwarfs is more likely affected by Type II rather than Type Ia SNe.

Comparing the derived chemical properties of the simulated galaxies with those of the observed UFDs (CVn II, Leo IV, Coma Berenices, Bootes I, Hercules, Segue I, UMa I, and UMa II), we find that all these UFDs appear to have experienced truncated star formation. Especially, the chemical properties of four UFDs, CVn II, Hercules, Coma Berenices, and Bootes I, tend to be consistent with those of the simulated analogs, HALO2 and HALO3, possibly implying that star formation in these UFDs was entirely quenched by reionization. The presence of relatively high metallicity stars in Leo IV and Segue I might be associated with bursts of star formation at late epochs after reionization, as suggested in HALO4 and HALO5. Furthermore, we estimate the time at which the most metal-rich stars of UMa II were generated, which allows us to infer the end of star formation in UMa II at $z \sim 3$. If we assume that this quenching of star formation in UMa II was correlated with gas stripping while infalling onto the MW halo, the estimated infall time of UMa II could be $t_{\text{infall}} \sim 11$ Gyr.

A key prediction of our simulations is the presence of extremely low-metallicity stars, with $[\text{Fe}/\text{H}] \lesssim -4$, in the local UFDs. These stars should preserve pure

Pop III signatures, i.e. enhanced carbon and alpha abundances, as a consequence of external metal-enrichment and the build-up of dwarfs via mergers. To date, such extremely low-metallicity stars have not yet been detected in UFDs, but they should come within reach over the next decade, with the advent of a number of next-generation telescopes. Among them is the Large Synoptic Survey Telescope (LSST) with its unprecedented wide-field imaging capability, ideally suited for detecting low surface-brightness systems. In addition, the greatly improved spectroscopic sensitivities of the upcoming extremely large ground-based telescopes, the Giant Magellan Telescope (GMT), the Thirty Meter Telescope (TMT), and the European Extremely Large Telescope (E-ELT), will revolutionize chemical abundance studies in the Local Group. Also, a recent study of the most metal-poor damped Lyman- α (DLA) system at $z \sim 3$, with an iron abundance of $[\text{Fe}/\text{H}] \lesssim -2.81$, suggests that the chemical signatures from a core-collapse supernova of a $20.5 M_{\odot}$ Pop III star are imprinted on the

observed DLA, indicating that such systems could be the predecessors of UFDs (Cooke et al. 2017). All these avenues promise to offer fundamental insights into the nature of the first generation of stars and into the metal enrichment history of the early Universe.

We are grateful to Volker Springel, Joop Schaye, and Claudio Dalla Vecchia for letting us use their versions of GADGET and their data visualization and analysis tools. Many thanks to Jun-Hwan Choi for discussion of the simulation set up. Also, we would like to thank to Yumi Choi, Lauren Corlies, and Jason Tumlinson for a fruitful discussion on results. The simulations were performed with the Texas Advanced Computing Center (TACC) at The University of Texas at Austin for providing HPC resources under XSEDE allocation TG-AST160038 (PI's M. Jeon). The authors acknowledge the El Gato cluster at the University of Arizona, which is funded by the National Science Foundation through Grant No. 1228509. VB was supported by NSF grant AST-1413501.

REFERENCES

- Abel, T., Anninos, P., Zhang, Y., & Norman, M. L. 1997, *New Astron.*, 2, 181
- Abel, T., Bryan, G. L., & Norman, M. L. 2002, *Science*, 295, 93
- Aoki, W., Beers, T. C., Christlieb, N., et al. 2007, *ApJ*, 655, 492
- Barris, B. J., & Tonry, J. L. 2006, *ApJ*, 637, 427
- Beers, T. C., & Christlieb, N. 2005, *ARA&A*, 43, 531
- Behroozi, P. S., Wechsler, R. H., & Conroy, C. 2013, *ApJ*, 770, 57
- Bland-Hawthorn, J., Sutherland, R., & Webster, D. 2015, *ApJ*, 807, 154
- Bovill, M. S., & Ricotti, M. 2009, *ApJ*, 693, 1859
- . 2011, *ApJ*, 741, 18
- Boylan-Kolchin, M., Weisz, D. R., Johnson, B. D., et al. 2015, *MNRAS*, 453, 1503
- Bradford, J. D., Geha, M. C., & Blanton, M. R. 2015, *ApJ*, 809, 146
- Bromm, V. 2013, *Rep. Prog. Phys.*, 76, 112901
- Bromm, V., Coppi, P. S., & Larson, R. B. 2002, *ApJ*, 564, 23
- Bromm, V., Kudritzki, R. P., & Loeb, A. 2001, *ApJ*, 552, 464
- Bromm, V., & Yoshida, N. 2011, *ARA&A*, 49, 373
- Brook, C. B., Di Cintio, A., Knebe, A., et al. 2014, *ApJL*, 784, L14
- Brown, T. M., Tumlinson, J., Geha, M., et al. 2012, *ApJL*, 753, L21
- . 2014, *ApJ*, 796, 91
- Bullock, J. S., Kravtsov, A. V., & Weinberg, D. H. 2000, *ApJ*, 539, 517
- Chatzopoulos, E., & Wheeler, J. C. 2012, *ApJ*, 748, 42
- Cooke, R. J., & Madau, P. 2014, *ApJ*, 791, 116
- Cooke, R. J., Pettini, M., & Steidel, C. C. 2017, *MNRAS*, arXiv:1701.03103
- Corlies, L., Johnston, K. V., Tumlinson, J., & Bryan, G. 2013, *ApJ*, 773, 105
- Dalla Vecchia, C., & Schaye, J. 2012, *MNRAS*, 426, 140
- Durier, F., & Dalla Vecchia, C. 2012, *MNRAS*, 419, 465
- Fan, X., Strauss, M. A., Becker, R. H., et al. 2006, *AJ*, 132, 117
- Ferland, G. J., Korista, K. T., Verner, D. A., et al. 1998, *PASP*, 110, 761
- Fitts, A., Boylan-Kolchin, M., Elbert, O. D., et al. 2016, arXiv:1611.02281, arXiv:1611.02281
- Förster, F., Wolf, C., Podsiadlowski, P., & Han, Z. 2006, *MNRAS*, 368, 1893
- Frebel, A., & Bromm, V. 2012, *ApJ*, 759, 115
- Frebel, A., Norris, J. E., Gilmore, G., & Wyse, R. F. G. 2016, *ApJ*, 826, 110
- Frebel, A., Simon, J. D., Geha, M., & Willman, B. 2010, *ApJ*, 708, 560
- Frebel, A., Simon, J. D., & Kirby, E. N. 2014, *ApJ*, 786, 74
- Gardner, J. P., et al. 2006, *Space Sci. Rev.*, 123, 485
- Garrison-Kimmel, S., Bullock, J. S., Boylan-Kolchin, M., & Bardwell, E. 2016, arXiv:1603.04855, arXiv:1603.04855
- Geha, M., Blanton, M. R., Yan, R., & Tinker, J. L. 2012, *ApJ*, 757, 85
- Gilmore, G., Norris, J. E., Monaco, L., et al. 2013, *ApJ*, 763, 61
- Glover, S. C. O., & Jappsen, A.-K. 2007, *ApJ*, 666, 1
- Gnedin, N. Y., & Kravtsov, A. V. 2006, *ApJ*, 645, 1054
- Governato, F., Weisz, D., Pontzen, A., et al. 2015, *MNRAS*, 448, 792
- Grebel, E. K., & Gallagher, III, J. S. 2004, *ApJL*, 610, L89
- Greif, T. H., Johnson, J. L., Klessen, R. S., & Bromm, V. 2009, *MNRAS*, 399, 639
- Griffen, B. F., Dooley, G. A., Ji, A. P., et al. 2016, arXiv:1611.00759, arXiv:1611.00759
- Gunn, J. E., & Peterson, B. A. 1965, *ApJ*, 142, 1633
- Haardt, F., & Madau, P. 2011, arXiv:1103.5226, arXiv:1103.5226
- . 2012, *ApJ*, 746, 125
- Hahn, O., & Abel, T. 2011, *MNRAS*, 415, 2101
- Haiman, Z., Thoul, A. A., & Loeb, A. 1996, *ApJ*, 464, 523
- Heger, A., & Woosley, S. E. 2002, *ApJ*, 567, 532
- . 2010, *ApJ*, 724, 341
- Hirano, S., Hosokawa, T., Yoshida, N., Omukai, K., & Yorke, H. W. 2015, *MNRAS*, 448, 568
- Hirano, S., Hosokawa, T., Yoshida, N., et al. 2014, *ApJ*, 781, 60
- Hopkins, P. F., Kereš, D., Oñorbe, J., et al. 2014, *MNRAS*, 445, 581
- Hosokawa, T., Hirano, S., Kuiper, R., et al. 2016, *ApJ*, 824, 119
- Hosokawa, T., Omukai, K., Yoshida, N., & Yorke, H. W. 2011, *Science*, 334, 1250
- Ishigaki, M. N., Aoki, W., Arimoto, N., & Okamoto, S. 2014, *A&A*, 562, A146
- Iwamoto, N., Umeda, H., Tominaga, N., Nomoto, K., & Maeda, K. 2005, *Science*, 309, 451
- Jeon, M., Bromm, V., Pawlik, A. H., & Milosavljević, M. 2015, *MNRAS*, 452, 1152
- Jeon, M., Pawlik, A. H., Bromm, V., & Milosavljević, M. 2014, *MNRAS*, 444, 3288
- Ji, A. P., Grebel, A., & Bromm, V. 2015, *MNRAS*, 454, 659
- Kirby, E. N., Cohen, J. G., Guhathakurta, P., et al. 2013, *ApJ*, 779, 102
- Kitayama, T., & Yoshida, N. 2005, *ApJ*, 630, 675
- Klessen, R. S., & Lin, D. N. 2003, *Physical Review E*, 67, 046311
- Kruijssen, J. M. D., & Mieske, S. 2009, *A&A*, 500, 785
- Kudritzki, R.-P., & Puls, J. 2000, *ARA&A*, 38, 613
- Mannucci, F., Della Valle, M., & Panagia, N. 2006, *MNRAS*, 370, 773
- Marigo, P. 2001, *A&A*, 370, 194
- McKee, C. F., & Tan, J. C. 2008, *ApJ*, 681, 771
- Meynet, G., Ekström, S., & Maeder, A. 2006, *A&A*, 447, 623
- Milosavljević, M., & Bromm, V. 2014, *MNRAS*, 440, 50
- Munshi, F., Governato, F., Brooks, A. M., et al. 2013, *ApJ*, 766, 56
- Muratov, A. L., Gnedin, O. Y., Gnedin, N. Y., & Zemp, M. 2013, *ApJ*, 773, 19
- Norris, J. E., Yong, D., Bessell, M. S., et al. 2013, *ApJ*, 762, 28
- Oñorbe, J., Boylan-Kolchin, M., Bullock, J. S., et al. 2015, *MNRAS*, 454, 2092
- Omukai, K. 2000, *ApJ*, 534, 809
- Portinari, L., Chiosi, C., & Bressan, A. 1998, *A&A*, 334, 505
- Revaz, Y., Arnaudon, A., Nichols, M., Bonvin, V., & Jablonka, P. 2016, *A&A*, 588, A21
- Revaz, Y., Jablonka, P., Sawala, T., et al. 2009, *A&A*, 501, 189
- Ricotti, M., & Gnedin, N. Y. 2005, *ApJ*, 629, 259

- Ricotti, M., Parry, O. H., & Gnedin, N. Y. 2016, *ApJ*, 831, 204
- Ritter, J. S., Safrank-Shrader, C., Gnat, O., Milosavljević, M., & Bromm, V. 2012, *ApJ*, 761, 56
- Rocha, M., Peter, A. H. G., & Bullock, J. 2012, *MNRAS*, 425, 231
- Safrank-Shrader, C., Montgomery, M. H., Milosavljević, M., & Bromm, V. 2016, *MNRAS*, 455, 3288
- Saitoh, T. R., & Makino, J. 2009, *ApJ*, 697, L99
- Salvadori, S., & Ferrara, A. 2009, *MNRAS*, 395, L6
- Salvadori, S., Skúladóttir, Á., & Tolstoy, E. 2015, *MNRAS*, 454, 1320
- Sawala, T., Scannapieco, C., Maio, U., & White, S. 2010, *MNRAS*, 402, 1599
- Schaerer, D. 2002, *A&A*, 382, 28
- Schmidt, M. 1959, *ApJ*, 129, 243
- Schneider, R., & Omukai, K. 2010, *MNRAS*, 402, 429
- Shen, S., Madau, P., Conroy, C., Governato, F., & Mayer, L. 2014, *ApJ*, 792, 99
- Simon, J. D., Frebel, A., McWilliam, A., Kirby, E. N., & Thompson, I. B. 2010, *ApJ*, 716, 446
- Simpson, C. M., Bryan, G. L., Johnston, K. V., et al. 2013, *MNRAS*, 432, 1989
- Smith, B. D., Wise, J. H., O'Shea, B. W., Norman, M. L., & Khochfar, S. 2015, *MNRAS*, 452, 2822
- Springel, V. 2005, *MNRAS*, 364, 1105
- Springel, V., White, S. D. M., Tormen, G., & Kauffmann, G. 2001, *MNRAS*, 328, 726
- Stacy, A., Bromm, V., & Lee, A. T. 2016, *MNRAS*, 462, 1307
- Stacy, A., Greif, T. H., & Bromm, V. 2012, *MNRAS*, 422, 290
- Stierwalt, S., Besla, G., Patton, D., et al. 2015, *ApJ*, 805, 2
- Susa, H., Hasegawa, K., & Tominaga, N. 2014, *ApJ*, 792, 32
- Tegmark, M., Silk, J., Rees, M. J., et al. 1997, *ApJ*, 474, 1
- Thielemann, F.-K., Argast, D., Brachwitz, F., et al. 2003, in *From Twilight to Highlight: The Physics of Supernovae*, ed. W. Hillebrandt & B. Leibundgut, 331
- Tinsley, B. M. 1979, *ApJ*, 229, 1046
- Tolstoy, E., Hill, V., & Tosi, M. 2009, *ARA&A*, 47, 371
- Umeda, H., & Nomoto, K. 2003, *Nature*, 422, 871
- Vargas, L. C., Geha, M., Kirby, E. N., & Simon, J. D. 2013, *ApJ*, 767, 134
- Webster, D., Bland-Hawthorn, J., & Sutherland, R. 2015, *ApJ*, 799, L21
- Webster, D., Sutherland, R., & Bland-Hawthorn, J. 2014, *ApJ*, 796, 11
- Weisz, D. R., Dolphin, A. E., Skillman, E. D., et al. 2014, *ApJ*, 789, 148
- Wetzel, A. R., Deason, A. J., & Garrison-Kimmel, S. 2015, *ApJ*, 807, 49
- Wheeler, C., Oñorbe, J., Bullock, J. S., et al. 2015, *MNRAS*, 453, 1305
- Wiersma, R. P. C., Schaye, J., Theuns, T., Dalla Vecchia, C., & Tornatore, L. 2009, *MNRAS*, 399, 574
- Wise, J. H., Turk, M. J., Norman, M. L., & Abel, T. 2012, *ApJ*, 745, 50
- Yong, D., Norris, J. E., Bessell, M. S., et al. 2013, *ApJ*, 762, 27